

# Geochemistry, Geophysics, Geosystems

## RESEARCH ARTICLE

10.1029/2019GC008720

### Key Points:

- InSAR analysis reveals up to 25 cm (peak rate ~6 mm/day) line of sight inflation during seismic swarms at Semisopchnoi Volcano, Alaska
- Relocation of seismic events from the 2014 and 2015 volcanic swarms reveals linear trends defining an aseismic zone under the caldera
- Inflation is modeled with a 4-km-wide SE-dipping prolate spheroid beneath the caldera at a depth of 8 km bsl

### Supporting Information:

- Supporting Information S1
- Table S1
- Table S2
- Table S3
- Table S4
- Table S5
- Table S6
- Table S7
- Table S8
- Table S9
- Table S10

### Correspondence to:

K. G. DeGrandpre,  
kdegrandpre@smu.edu

### Citation:

DeGrandpre, K. G., Pesicek, J. D., Lu, Z., DeShon, H. R., & Roman, D. C. (2019). High rates of inflation during a noneruptive episode of seismic unrest at Semisopchnoi Volcano, Alaska in 2014–2015. *Geochemistry, Geophysics, Geosystems*, 20. <https://doi.org/10.1029/2019GC008720>

Received 20 SEP 2019

Accepted 11 DEC 2019

Accepted article online 15 DEC 2019

©2019. American Geophysical Union.  
All Rights Reserved.

## High Rates of Inflation During a Noneruptive Episode of Seismic Unrest at Semisopchnoi Volcano, Alaska in 2014–2015

Kimberly G. DeGrandpre<sup>1</sup>, Jeremy D. Pesicek<sup>2</sup>, Zhong Lu<sup>1</sup>, Heather R. DeShon<sup>1</sup>, and Diana C. Roman<sup>3</sup>

<sup>1</sup>Huffington Department of Earth Sciences, Southern Methodist University, Dallas, Texas, USA, <sup>2</sup>U.S. Geological Survey Volcano Disaster Assistance Program, Volcano Science Center, Vancouver, Washington, USA, <sup>3</sup>Department of Terrestrial Magnetism, Carnegie Institution for Science, Washington, District of Columbia, USA

**Abstract** Magma intrusion rate is a key parameter in eruption triggering but is poorly quantified in existing geodetic studies. Here we examine two episodes of rapid inflation in this context. Two noneruptive microseismic swarms were recorded at Semisopchnoi Volcano, Alaska in 2014–2015. We use differential SAR techniques and TerraSAR-X images to document surface deformation from 2011 to 2015, which comprises island-wide radial inflation totaling ~25 cm (+/–1 cm) line of sight displacement in 2014–2015. Multiple source geometries are tested in an inversion of the deformation data, and InSAR data are best fit by a spheroid trending to the northeast and plunging to the southeast, with a major axis of ~4 km and minor axes of ~1 km, directly under the central caldera of Semisopchnoi. In 2014, a modeled influx of 0.043 km<sup>3</sup> of magma caused line of sight displacement of ~17 cm. This magma was stored at a depth of ~8 km, until 2015 when 0.029 km<sup>3</sup> was added. Along with the definition of inflation source parameters, the recorded seismic events are relocated using differential travel times. These relocated events outline a linear aseismic area within a larger zone of shallow (<10 km) seismicity. This aseismic region aligns with the centroid of the deformation model. Based on these geodetic and seismic models, the plumbing system at Semisopchnoi is interpreted as a spheroidal magma storage zone at a depth of ~8 km below a linear feature of partial melt. The observed deformation and seismicity appear to result from rapid injection into this main storage region.

## 1. Introduction

Developing an unbiased understanding of processes occurring throughout the life cycles of volcanoes globally is a key outstanding challenge in volcanology (NASEM, 2017; Reath et al., 2019). Most studies of volcanism focus on the eruptive phase of the volcanic life cycle; however, there is increasing evidence that intereruptive processes such as crustal magma intrusion are common and may control or influence eruption parameters such as timing, duration, type, and magnitude (e.g., Biggs & Pritchard, 2017; Biggs et al., 2014; Moran et al., 2011). Furthermore, distinguishing episodes of unrest that do not immediately culminate in eruption from those that are truly precursory is a major challenge in volcano monitoring. One hypothesis is that the rate of crustal magma intrusion is a key control on whether or not an intrusion will proceed to eruption (Degruyter & Huber, 2014; Stix & de Moor, 2018). Thus, placing quantitative upper bounds on the rate at which magma can be emplaced in the crust without triggering an eruption is crucial.

Arc volcanoes can erupt without associated surface deformation (e.g., Fournier et al., 2010; Lu et al., 2007; Lu & Dzurisin, 2014; Moran et al., 2006; Pritchard et al., 2018), but they commonly exhibit episodes of inflation that culminate in an eruption. Establishing records of an individual volcano's deformation “baseline” with InSAR measurements of the direction, shape, rate, and magnitude of displacement as well as nondeforming periods is essential for hazard mitigation (e.g., Ebmeier et al., 2018; Lu et al., 2007; Lu & Dzurisin, 2010, 2014; Pritchard et al., 2018; Reath et al., 2019). Episodes of inflation have been observed to extend through months or even years with rates of 10 s–100 s mm/yr, but the precise nature of the relationship between displacement and parameters that describe eruptive activity has not yet been defined (e.g., DeGrandpre et al., 2017; Lee et al., 2013; Lu & Dzurisin, 2010; Pritchard et al., 2018). However, surface deformation that exceeds these rates commonly terminates with an eruption, except in cases of large caldera systems, such as Campi Flegrei or Laguna del Maule, where respective inflation rates of up to 90 and 40 cm/yr have been

observed (Acocella et al., 2015; Le Mével et al., 2015). It is unprecedented to observe rapid, large magnitude (tens of centimeters), inflation at an arc volcano without an ensuing eruption.

In this study, we examine surface deformation and seismicity associated with two episodes of volcanic unrest in 2014 and 2015 at Semisopochnoi Island, Alaska. We document a minimum estimate of surface uplift of 25 cm over 2 years, a high rate and magnitude of deformation for a noneruptive episode at an island arc volcano. Synthetic aperture radar (SAR) images collected by the German TerraSAR-X satellite are differenced using Interferometric SAR (InSAR) techniques to create interferograms of relative surface displacement. A nonlinear least-squares inversion for deformation source parameters that define the geometries of the Mogi point source (Mogi, 1958), Okada dislocation plane (Okada, 1985), and Yang spheroid (Yang et al., 1988) is performed in order to estimate the magma source location and volume change responsible for the observed surface deformation. We also highlight the shortcomings of current InSAR processing, subsampling, and error estimation techniques as applied to remote volcanoes with island wide deformation, a single viewing geometry, lacking turbulent atmospheric models, and severe temporal limitations.

Using relative relocation methods (Waldhauser, 2001; Waldhauser & Ellsworth, 2000; Zhang & Thurber, 2003, 2006), the Alaska Volcano Observatory (AVO) seismic event catalog from 2014 to 2015 is also relocated to more precisely define the spatial distribution of seismic event locations at Semisopochnoi Volcano as they relate spatially to surface deformation. This work also illustrates limitations of tomographic inversions created from observations of shallow events recorded by small seismic networks. Finally, the geodetic and seismic models produced in this study are integrated with previously published geochemical analyses (Coombs et al., 2018) in the first multidisciplinary assessment of the plumbing system at Semisopochnoi.

## 2. Background

The easternmost extension of the United States and North America by longitude is Semisopochnoi Island (179.58°E), a remote and uninhabited volcanic island that is part of the Rat Island group in the western Aleutian island arc (Figure 1). The western Aleutian volcanoes are relatively younger and smaller than their eastern counterparts (Scholl et al., 1986), and Semisopochnoi is the largest of these younger volcanoes, with an approximate diameter of 20 km. Surface features of Semisopochnoi are largely dominated by the main caldera centrally located on the island, with a diameter of ~8 km (Figure 1). Polygenetic stratovolcanoes and monogenetic cones surround the main crater rim and exhibit varying compositions of basalt, andesite, and dacite (Coats, 1959; Coombs et al., 2018).

The western Aleutian arc is primarily influenced by complex north-west oblique subduction of the Pacific plate beneath the Bering plate. The tectonic stress regime at Semisopochnoi is potentially further complicated by local effects associated with its location on the southern extent of an abandoned subduction trench, Bowers Ridge (Cooper et al., 1981; Kienle, 1971; Ludwig et al., 1971; Rabinowitz, 1974; Scholl et al., 1986; Wanke et al., 2012; Figure 1). The Bering plate rotates clockwise around a Euler pole located at 42.5°N, 121.3°E with an angular speed of 6.0°/Ma (Cross & Freymueller, 2008). This rotation creates complicated subduction angles that begin to shear the Aleutian arc in the west as the boundary evolves from convergent to transform. Geist et al. (1988) define a system of five blocks with independent clockwise rotation along the Aleutian arc from geologic, magnetic, and seismic studies. The Rat Islands block is described as having northeast-southwest trending linear features with extensional and strike-slip motion evident in seismic reflection profiles. These stress regimes are described independently using GPS and block models by Cross and Freymueller (2008).

Trends in tholeiitic differentiation and the relatively large erupted volumes at Semisopochnoi volcano are indicative of relatively fast magma ascent through fractured lithosphere (Grosse et al., 2014). These tholeiitic eruptions reflect segmentation boundary volcanism due to the extensional rotating block, as well as the intersection of Bowers Ridge with the Aleutian trench (Coats, 1959; Coombs et al., 2018; Delong et al., 1985; Geist et al., 1988). The only confirmed eruptions occurred in 1873 from the Mount Cerberus three cone complex, but in 1987 eyewitness accounts indicate a potential eruption from Sugarloaf Peak. Four eruptions are suspected to have occurred in the last century from the polygenetic stratocone Mount Cerberus, Sugarloaf Peak, and the monogenetic Lakeshore cone (Coats, 1959; Coombs et al., 2018).

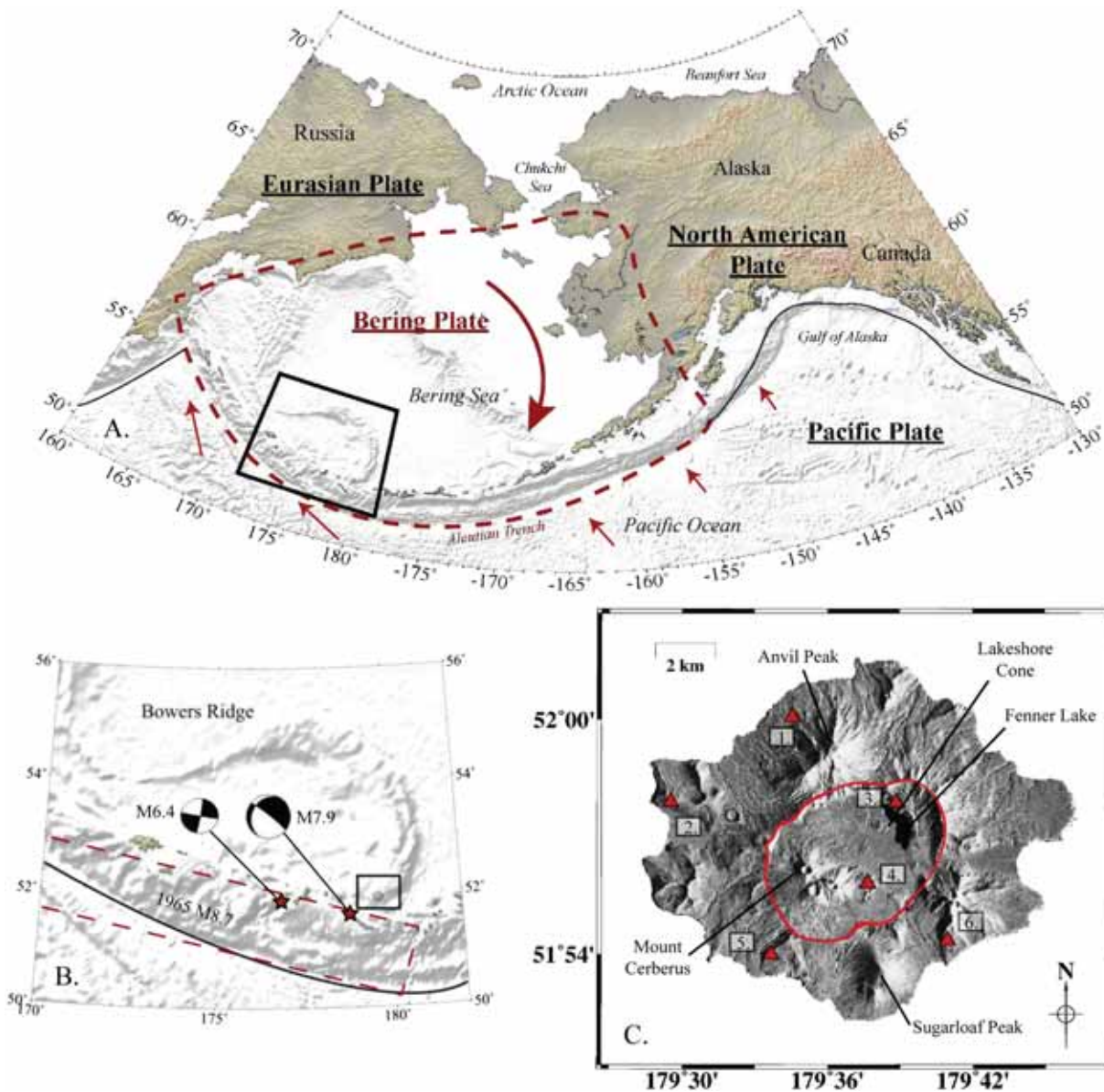


**Figure 1.** Tectonic location map of the Aleutian Island Arc (a), with the Bering plate outlined in red dashed lines and clockwise rotation indicated with bold red arrow (Cross & Freymueller, 2008). Pacific plate motion is indicated with red arrows that show increasing rate and obliquity to the west. Outlined black box (a) indicates the Rat Island group (b). Red dashed region in (b) outlines the rupture zone of the 1965 M8.7 earthquake, and epicenters and focal mechanisms for the 2014 M7.9 and M6.4 are plotted. Semisopchnoi is outlined with a black box. The abandoned subduction trench, Bowers Ridge, is also prominent to the north of Semisopchnoi (black box). SAR intensity image of Semisopchnoi (c) shows locations of the six seismic stations, CEAP (1.), CETU (2.), CEPE (3.), CERB (4.), CESW (5.), and CERA (6.). The prominent and recent eruptive peaks, Lakeshore Cone, Anvil, Sugarloaf, and the Mount Cerberus cone complex as well as Fenner Lake are labeled. The caldera is outlined by a solid red line.

There have been no observations of volcanic activity at Semisopchnoi for the past three decades, and the most notable events have been limited to earthquake rupture along the Aleutian trench. For this reason, the sudden onset of volcanic seismic activity in 2014 was unusual and is described in Cameron et al. (2017) and summarized as follows. In the summer of 2014 and the early spring of 2015, AVO seismometers on Semisopchnoi and surrounding islands (Figure 1) recorded elevated levels of seismic activity. The seismic network, installed in 2005, had only recorded a low (background) rate of local seismic events prior to the 2014 activity. The 2014–2015 microseismic events (magnitudes of  $-0.7$ – $2.8$ ) were primarily located at upper crustal depths ( $<10$  km bsl), but neither swarm resulted in a volcanic eruption (Cameron et al., 2017; Dixon et al., 2017). Five of the six seismic stations on Semisopchnoi were operational when low frequency seismic

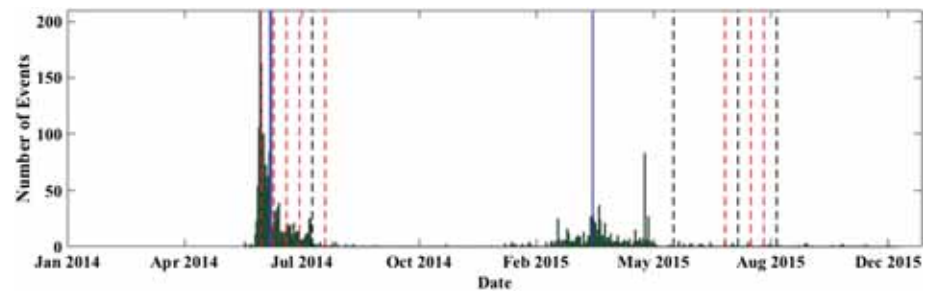


**Figure 2.** Green histograms show the number of daily seismic events at Semisopchnoi Island from the beginning of 2014 to the end of 2015. Dates of acquired SAR images are plotted as red dashed lines (good quality) and black dashed lines (poor quality). The solid blue lines indicate the 2014 date of the M7.9 earthquake and the 2015 initial tremor report (25 March 2015).

events were first observed on 1 June 2014. On 9 June, the seismic swarm, comprised mainly of high-frequency earthquakes, began, and volcanic tremor was

first noted on 12 June. By 13 June, the number of daily events was greater than double than that of the three previous days. The number of daily events reached a maximum (223; all high frequency) on 14 June 2014 (Figure 2). Following this peak in activity, the number of daily events decreased to 20–30 by the end of June and continued to decline to background levels by early September 2014. The cumulative magnitude of the 2014 seismic activity is  $\sim$ M3.2. An M7.9 oblique-extensional earthquake occurred on 23 June 2015, 73 km southwest of Semisopchnoi at 100 km bsl (Figure 1) and appeared to have no effect on Semisopchnoi's seismic activity. A M6.4 strike-slip aftershock occurred the next day in the same region of the 1965 M8.4 rupture zone (Figure 1). These larger tectonic events follow the stress regime and expected motion defined in the Geist et al. (1988) block models.

In January 2015 microseismic unrest was once again detected at Semisopchnoi, and the number of daily events increased until 20 March 2015 (Figure 2) with episodes of volcanic tremor recorded on 25 March (Dixon et al., 2017). After March 2015 there was a decline in frequency and intensity until early April 2015 when the volcano returned to a state of quiescence (Dixon et al., 2017). The total amount of seismic energy released during these four months ( $\sim$ M3.2) is similar to that of the June–July 2014 swarm, with events located in the same upper-crustal region below the center of the island (Dixon et al., 2017).

There are no GPS stations located at Semisopchnoi Island, and only one other study (Lu & Dzurisin, 2014) has published InSAR images of Semisopchnoi. These interferograms were generated from Envisat images acquired between 2004 and 2010. They appear to exhibit up to  $\sim$ 1 cm/yr of subsidence located only at the Mount Cerberus cone complex, while the majority of the island is nondeforming. The limited spatial extent of deformation in that study and the differences between ascending and descending images of the magnitude of deformation on the north-flank of Mount Cerberus indicated a shallow, localized deformation source possibly resulting from mechanisms such as thermoelastic contraction, mechanical compaction, or even gravitational sliding.

### 3. InSAR Analysis

#### 3.1. SAR Images and Processing

TerraSAR-X data (wavelength = 3.11 cm) descending pass images with a steep look angle of  $45^\circ$  are acquired every 11 days over Semisopchnoi, but due to snow cover, and thereby loss of coherence, only 17 images from summer months can be used to study surface displacements during 2011–2015 (Figure 2). GAMMA software is used to process these data and resolve deformation (Lu et al., 2005; Lu & Dzurisin, 2010; Wegmuller, 1997; Wegmuller et al., 1998). The images are differenced from each other to create 136 interferograms where the primary image is always an earlier date than the secondary image. GAMMA's adaptive filter (ADF) is then used to filter all of the interferograms in their original SAR coordinates before they are geocoded into map coordinates and filtered a second time in map coordinates, again using the ADF algorithm, and finally phase unwrapped (Table S1 in the supporting information; Lu,

Masterlark, & Dzurisin, 2005, Lu & Dzurisin, 2010; Wegmuller, 1997; Wegmuller et al., 1998). Observed deformation is radial and island-wide, and the gradient is consistent in all directions (the 136 unwrapped interferograms are available in the data repository; see Acknowledgments). The lengths of the perpendicular baselines are relatively short, with a maximum of 217 m and a mean of 14 m (Figure S1) so island-wide deformation is not expected to result from perpendicular baseline error based on the pair-wise logic (Massonnet & Feigl, 1998).

Two images from Sentinel-1 and seven images from ALOS-2 were also obtained. The two Sentinel-1 images were used to generate one interferogram (Figure S2), but unfortunately from the seven available ALOS-2 images, only one coherent interferogram was produced (Figure S3). These two interferograms are during periods when there was no seismic activity, and they both show no deformation but include topography-related atmospheric noise. These images are not used in any of the models because of their lack of deformation but are included in Supporting Information (Figures S2 and S3) because their temporal resolution provides additional constraints on when deformation was not occurring, and they provide constraints on the error introduced by topography-correlated atmospheric noise into interferograms showing uplift.

It is important to note that when an interferogram is generated, LOS displacements are given as relative measurements, not absolute measurements. Generally, this is not an issue, because the reference point is established as a pixel far from the deforming area that is considered to be stable. However, due to the island-wide nature of the observed deformation at Semisopochnoi, a stable reference pixel is unavailable, and the reference pixel (chosen as the farthest west pixel with coherence) is often undergoing deformation as well. Therefore, the measured LOS displacements are underestimating the actual surface deformation by the unknown magnitude of displacement that is occurring at this “stable” pixel. Each interferogram will also have a different ratio between the maximum LOS displacement and the displacement at this “stable” pixel because the deformation gradient does not remain constant in time, so the offset between measured LOS displacement and actual surface deformation is not constant across all interferograms.

The interferograms created from images acquired in 2014 do not span the entirety of the seismic swarm events, but instead begin on 15 June 2014, 15 days into the swarm. The coherent images from 2015 are acquired long after the 2015 seismic swarm had stopped (Figure 2). Deformation during the later stages of the 2014 seismic swarm and the entirety of the 2015 seismic swarm can thus only be estimated using year-long interferograms. Because of the poor temporal resolution of the deformation periods, we did not expect time series analysis to provide any additional use, nevertheless the method was tested using both the GAMMA program MB and the small baseline subset (SBAS) method (Berardino et al., 2002) that has been applied at other volcanoes (Biggs et al., 2010; Lee et al., 2006; Lundgren et al., 2004). These methods produce a time series of cumulative deformation for each image acquisition date using pixels that are coherent in each of the interferograms used in the inversion. In an effort to preserve coherence during this process, interferograms were assembled into smaller groups that isolate distinct deformation periods based on their temporal range, identified as “pre-2014,” “2014,” “2015,” and “2014–2015” (Table S2 and Figures S4–S7). Because no satellite acquisition dates are concurrent with the majority of the deformation, the use of a 1-year interferogram (Figures S5 and S6) is necessary for both the 2014 and 2015 time series generation. This reduces the number of coherent pixels available for time series inversion and unfortunately eliminates the deformation signal in the center of the caldera and along the perimeter of the island (Figures S8 and S9). Because this loss of coherence in the center of the island results in loss of accumulated deformation, location of maximum displacement, and poor definition of the geometric pattern of that displacement, the application of time series inversion is not appropriate for our dataset and is not used further in this study (Figures S8 and S9).

While the images with long temporal baselines reduce coherence for time series generation, there is, nonetheless, a surprising amount of coherence for both long and short period interferograms due to the lack of tall vegetation on the island. A distinct period of significant inflation is temporally associated with the 2014 microseismic swarm and is most obvious in interferograms that span 11 August 2013 to 15 and 26 June 2014 (Figures 3a, 3d, 4, 5, and S5). Inflation continues into July, and little to no deformation is observed for the rest of the month as the seismic activity began to decline (Figures 3c, 3e, 3f, and S5). A small signal between the end of July and beginning of August 2014 is evident (Figures 3e, 3f, and S5) but has little contribution overall to the cumulative uplift across Semisopochnoi (~17.1 cm in the line of sight [LOS] direction

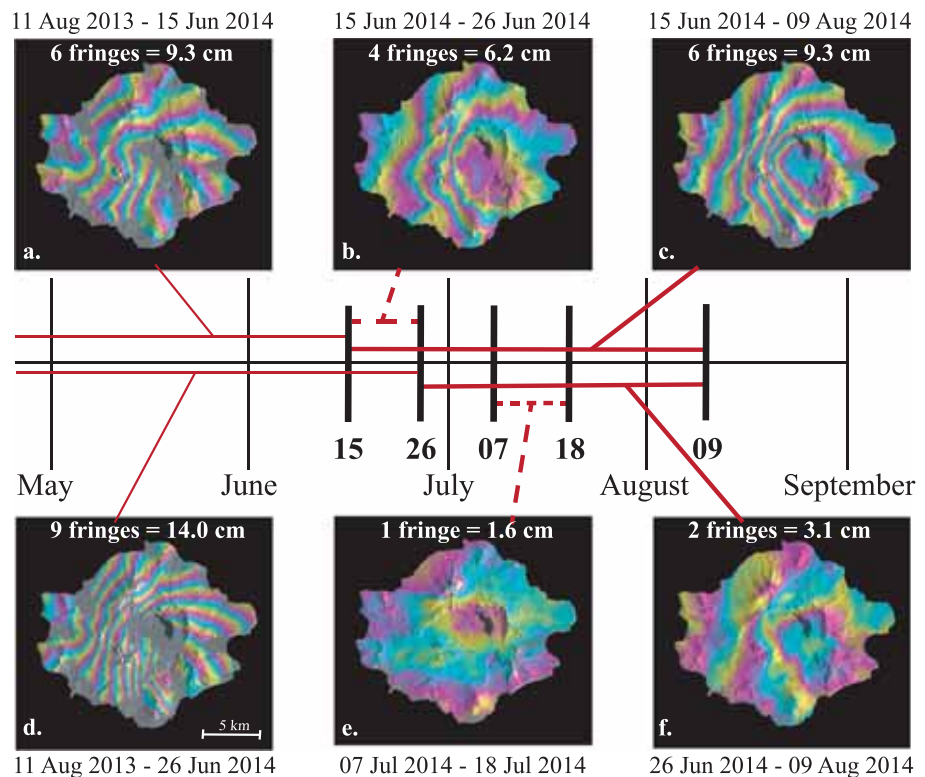


**Figure 3.** Timeline created from a selection of six (panels a.-f.) unwrapped interferograms from 2014. LOS deformation is consistently centered to the north of Sugarloaf Peak on the southeast edge of the caldera with a decrease in the deformation gradient towards the western edge of Semisopchnoi. Interferograms b. and f. have a combined magnitude of deformation equal to the deformation in interferogram c., which covers deformation over the total temporal span of the b. and f. interferograms. This phase closure illustrates the reliability of processing methods, coherence consistency, and a high signal to noise ratio (SNR) through consistent deformation patterns and magnitudes. The satellite azimuth is  $-170^\circ$  with a look angle of  $45^\circ$ , primary and secondary image acquisition dates are indicated above or below each interferogram, the top left (northwestern) corner of each interferogram has coordinates of  $(52.0453^\circ\text{N}, 179.4445^\circ\text{E})$ , all images are unwrapped, and each fringe represents 1.55 cm of LOS displacement. These conventions are applied to all interferograms (Figures 4, 5 and S4–S7). The entire set of images used for modeling can be found in Figures S4–S7.

from 11 August 2013 to 9 August 2014). The uplift observed in the late July–August interferograms is centered in the southeast corner of the caldera to the north of Sugarloaf Peak and the east of the Mount Cerberus cone complex. This asymmetric, radial inflation has an elongated shape that trends to the southeast/northwest so that the spatial pattern of the surface deformation appears to have a slight eccentricity, which could be an artifact of the steep look angle of the satellite. Gradients are largest to the west and decrease with distance from the point of maximum displacement that is at the center of the deformation pattern in every interferogram that exhibits displacement.

The seismic activity (See section 4 for detail) in 2015 began during late winter and continued into early spring, when the island was still covered in snow. Deformation directly associated with the swarm cannot be observed using SAR images during these winter months because of the loss of coherence. Instead, interferograms between August 2014 and the summer of 2015 are used to measure the cumulative surface deformation that occurred during that time frame (Figure S6). This long temporal baseline between images results in less coherent interferograms, even after the same ADFs used in 2014 are applied. The resulting interferograms do, however, retain a sufficient amount of coherence to observe deformation patterns similar to those measured in 2014 (Figure S6). The source of the 2015 inflation appears to have shifted to the southeast since 2014 and is positioned on the outside edge of the main caldera, south of Fenner Lake (Figures 1, 4, 5, and S6). The steeper surface deformation gradient to the west, decreasing with distance across the island, is also similar to the spatial pattern in the 2014 (Figures S5 and S6). The total LOS inflation across the island is  $\sim 7.8$  cm in 2015, which is slightly less than half of the measured LOS displacement in 2014 ( $\sim 17.1$  cm). The

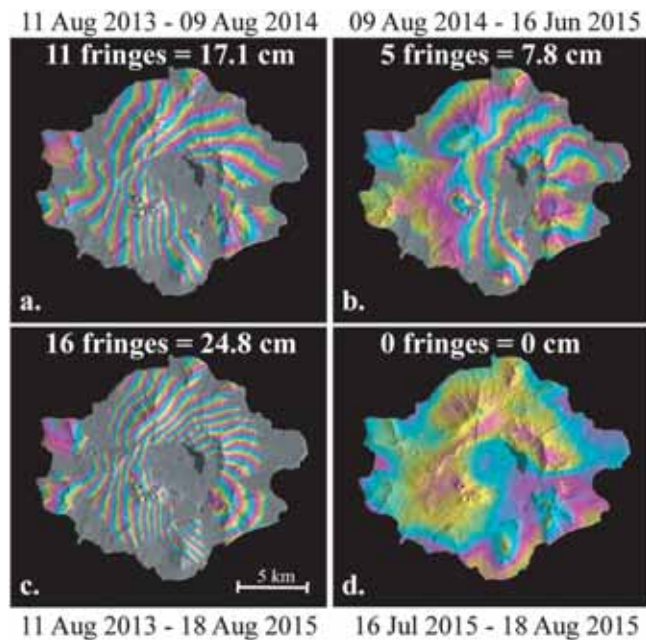


**Figure 4.** Total deformation for the year of 2014 (a) including the seismic swarm comes to  $\sim 17.1$  cm of uplift; this agrees with the sum of individual interferograms in Figure 3. In 2015 a total of five fringes ( $\sim 7.8$  cm of deformation) are observed across the island (b), which can be added to the total deformation for 2014 (a) for a 2-year total deformation of 24.9 cm. This is verified by the 2-year interferogram (c). By the summer of 2015, once seismic activity had ceased, deformation is not expected to be significant and the displacement signal is dominated by topography-correlated noise (d). The entire set of images used for modeling is included as supporting information (Figures S4–S7).

interferograms acquired in the summer of 2015 over several of the 11-day revisit periods exhibit little to no deformation, and the seismic activity during this time period is significantly lower than prior months (Figure 2).

This relatively extensive spatial coherence between calendar years extends to the 2-year period that involves both the 2014 and 2015 seismic swarms (Figures 4, 5, and S7). Not surprisingly, the shape and center location of the deformation is roughly the average of the 2 years individually and similarly the observed LOS uplift of  $\sim 24.8$  cm from 11 August 2013–07 August 2015 is essentially the same amount of LOS displacement seen in the independent 2014 and 2015 interferograms (17.1 and 7.8 cm, respectively).

Atmospheric error is a common, but poorly quantified, effect in the Aleutian Arc due to the localized and turbulent nature of atmosphere at small, isolated, volcanic islands (Lu & Dzurisin, 2014; Wang et al., 2018). Semisopochnoi presents particular difficulties in this respect, as topographic changes across the island are irregularly shaped, and the nearest ground-based weather stations are hundreds of kilometers away. The variability in local atmospheric weather can clearly be observed in nondeforming images from 2011 and 2015 (Figures S4 and S6, respectively) and in model residuals. Because these nondeforming interferograms vary in spatial pattern and magnitude, it is inappropriate to simply select one of these images and apply it as an atmospheric correction. Instead, we attempted to correct the interferograms for atmospheric error at Semisopochnoi using tropospheric modeling and semivariogram analysis.

Tropospheric delay estimations for each image acquisition date were obtained from the Iterative Tropospheric Decomposition (ITD) model (Yu et al., 2017) available through the GACOS system (Yu et al., 2018; Yu et al., 2018). The ITD model utilizes SRTM and ASTER DEMs in combination with the high resolution ( $0.125^\circ$ , 6-hr) weather models produced by the European Centre for Medium-Range Weather Forecasts (Figure S10). Unfortunately, these models do not provide adequate resolution for Semisopochnoi Island ( $\sim 0.310^\circ$  diameter), and the result is simply a topography-correlated atmospheric model that does not vary significantly in time. The maximum estimates of atmospheric delay from the ITD model are  $\sim 2.5$  mm (Figure S10), which is one order of magnitude less than the observed deformation, and thus not expected to influence model results.

Semivariogram analysis is another method commonly used to estimate covariance within a geospatial image under the assumption that errors in the data can be simulated using an exponential function (Webster & Oliver, 2007). This method can only be applied to nondeforming images because the purpose is to estimate covariance of the data noise and deformation would dominate the signal. Unfortunately, when this method was applied to the nondeforming interferograms from 2011 and 2015, it became clear that fitting an exponential function to the data was a subjective exercise, based on the user's selection or masking of specific areas of an interferogram that could not accurately depict the data (see Text S1, Figures S11–S15, and Table S3 for further details).

Semivariogram analysis is another method commonly used to estimate covariance within a geospatial image under the assumption that errors in the data can be simulated using an exponential function (Webster & Oliver, 2007). This method can only be applied to nondeforming images because the purpose is to estimate covariance of the data noise and deformation would dominate the signal. Unfortunately, when this method was applied to the nondeforming interferograms from 2011 and 2015, it became clear that fitting an exponential function to the data was a subjective exercise, based on the user's selection or masking of specific areas of an interferogram that could not accurately depict the data (see Text S1, Figures S11–S15, and Table S3 for further details).

Subsampling using quadtree analysis can sometimes be useful to eliminate atmospheric error, estimate covariance, and increase computational efficiency (Lohman & Simons, 2005). This technique was also found to be subjective (see Text S2, Figures S16–S18, and Tables S4 and S5 for further details). Quadtree model input values that determine the method (mean, median, or bilinear), variance threshold, and other important parameters such as the way variance is calculated or how many iterations are used, are completely user-defined. The input parameter values are also rarely published and relate to the spatial scale and magnitude of deformation in each individual image. When objective, standardized limits were applied to these interferograms, we produced deformation maps with varying spatial patterns and magnitudes of displacement that oversampled areas with coherence loss rather than the deformation. Additionally, comparison with the

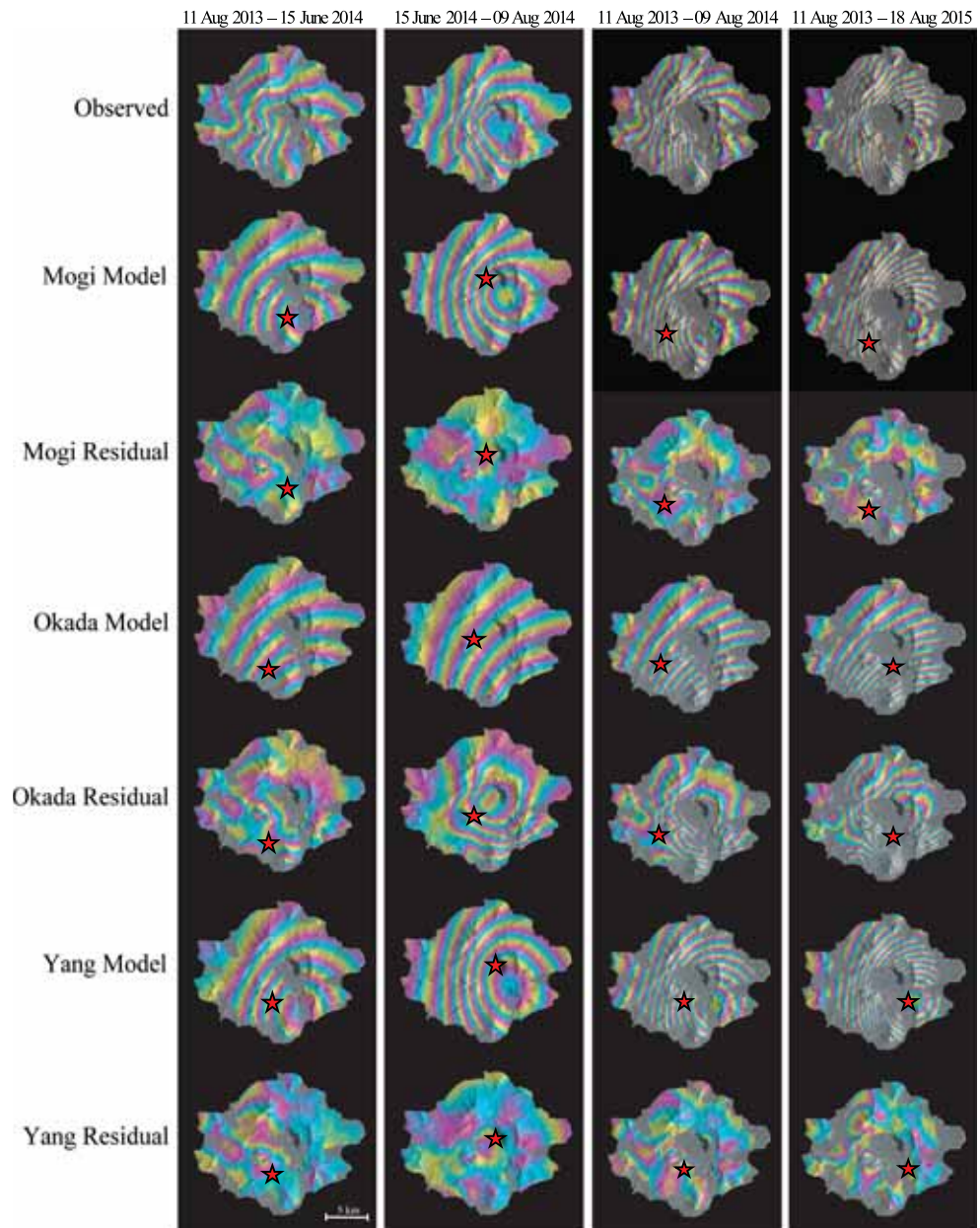


**Figure 5.** Comparison of surface deformation in processed interferograms (top row), synthetic model estimates, and their corresponding residuals during a sample of time periods during 2014. The primary and secondary image for each interferogram is indicated at the top, and the type of model is indicated on the left. The source location is indicated with a red star, and the associated model parameters can be found in Tables S6–S17.

original interferograms shows that the maximum deformation value estimated using quadtree methods is consistently higher than any of the interferogram measurements (Figure S18). While this method has been successfully applied at other locations, interferograms at Semisopchnoi are not ideal and the application of quadtree subsampling algorithms cannot be objectively, efficiently, and appropriately applied.

In summary, we are unable to accurately remove atmospheric effects from the interferograms presented in this study or to precisely quantify atmospheric error in the interferograms (generally the largest source of error). From nondeforming interferograms and model residuals, we estimate the atmospheric error to be on the order of 1 mm–1 cm and primarily dominated by turbulent effects. Techniques commonly applied to InSAR interferograms involving time series generation, atmospheric quantification, semivariogram

analysis, and subsampling are found to be inappropriate and thus not applied to this dataset (see Foster et al., 2013 and Kinoshita et al., 2013 for similar conclusions). This is to avoid the potential for bias or addition of unknown error to a dataset where uncertainty cannot be defined from the acquisition of the data, in the first place. Semisopochnoi is a data-limited case in which the magnitude, spatial extent, and timing of deformation are nonideal for these processing techniques. To compensate, we invert the full interferograms (see next section) rather than subsampled interferograms to take advantage of the high spatiotemporal coherence and to maximize constraints on geodetic models, resulting in the lowest error possible given the fundamental limitations of our dataset. We also note that estimates of atmospheric error appear to be sub centimeter, consistent with estimates of turbulent artifacts at similar volcanoes (e.g., Parker et al., 2015), and thus unlikely to make a significant difference in our results. Further studies to investigate the effects of an unstable reference point, subsampling bias, and turbulent atmospheric noise on deformation source parameters would be a valuable contribution to the field but are not within the scope of this study (see supporting information for additional discussion).

### 3.2. Inversion of Surface Deformation

The surface deformation at Semisopochnoi Volcano, observed in the processed interferograms, was analyzed through the inversion of LOS displacement measurements to define the best-fit deformation source parameters for three commonly used geometries (Lee et al., 2006, 2013; Lu et al., 2002, 2003, 2007; Lu & Dzurisin, 2010, 2014; Lu, Masterlark, & Dzurisin, 2005; Masterlark et al., 2012). The latitude, longitude, depth, source geometry, and pressure/volume change for a Mogi point source (Mogi, 1958), Yang spheroid (Yang et al., 1988), and Okada dislocation plane (Okada, 1985) were estimated in Matlab through a non-linear least squares inversion of Monte Carlo simulations limited by upper and lower bounded input parameters, using the “trust-region-reflective” optimization algorithm to minimize the residual sum of squares (RSS) with an error tolerance of 0.0001 and a maximum of 2,500 iterations for each simulation (DeGrandpre et al., 2017; Lu et al., 2002, 2003, 2007; Lu, Masterlark, & Dzurisin, 2005). Residuals are calculated by estimating the three-component displacement (east, north, and vertical) from the forward model predictions for each pixel in the interferogram, converting these directional displacements to LOS displacements, and then subtracting them from the LOS measurement available from every coherent pixel. Topographic model corrections (Williams & Wadge, 1998) were not made and are not expected to have a significant influence at Semisopochnoi where the average elevation is less than 500 m (maximum ~1,200 m at the summit of Anvil Mountain). Each interferogram is inverted independently for the deformation source parameters associated with each model. The advantage of using interferograms, as opposed to other geodetic techniques like GPS or tilt meters, is that they provide extensive spatial coverage of the study area, allowing for better definition of the latitude, longitude, and geometry of a deformation source through inversion modeling (Biggs et al., 2010). Unfortunately, the data are only for a single viewing geometry, so that the horizontal/vertical deformation ratio cannot be established and while InSAR is generally more sensitive to the vertical component of displacement, the data were obtained from a steep incidence angle (~45°), so horizontal deformation may have a measurable impact on the total LOS displacement. The depth and volume estimates of these models are thus nonunique, and the size and resolution of each image requires attention to computational efficiency, especially with large datasets, like that acquired here. To reduce computational cost, the interferograms were first analyzed visually those with low coherence or obvious errors from atmosphere or baseline noise were discarded, so that the total number of images used in the inversion was reduced from 136 to 66 (Table S1 and Figures S4–S7) and a limit of 25 Monte Carlo simulations was used for each image.

### 3.3. InSAR Surface Deformation Model Results

The deformation groups that were created to test time series analysis methods (section 3.1) were used to analyze deformation model results in order to preserve any source differences or progressions observed between the 2014 and 2015 seismic swarms (Table S2 and Figures S4–S7). This was done so that the best fitting model for each time frame could be independently averaged, and unique source parameters identified, providing a temporal as well as spatial evolution of this deformation source. The 2014 and 2015 groups were further subdivided into two sections to compare the difference between deformation associated with or independent of seismic activity. Tables 1–3 summarize the modeling best fit results for each time period, and the complete list of input interferograms, parameterization, and results can be found in Tables S6–S17. The inverse square

**Table 1**  
*Weighted Average Best Fit Mogi Model Parameters for Each Interferogram Group as Defined in Table S1*

Group	Longitude (dec. deg.)	Latitude (dec. deg.)	Depth (km)	Volume (km <sup>3</sup> )
Pre-2014	179.579	19.728	2.2	0.009
2014a	179.609	51.940	6.1	0.013
2014b	179.626	51.924	7.9	0.022
2015a	179.635	51.932	8.0	0.038
2015b	179.627	51.949	8.4	0.003
2014–2015	179.608	51.927	8.1	0.054

of the RSS value for each model is used as a weighting factor in the calculation of each group average so that ill-fit model parameters do not dominate the group average (Tables 1–3). This is performed under the premise that interferograms in each group reflect similar amounts of deformation.

The RSS values can only be used to compare the model fit of one geometry (Mogi, Okada, or Yang) for one interferogram and are not a valid tool for comparison between model geometries or interferograms. The Mogi model employs only four parameters, while the Yang and Okada models involve nine parameters, so that they have different degrees of freedom. Conventional statistical tests that evaluate the variance between models of different complexities cannot be applied to determine a better fit geometry due to the large amount of data points used to define each model.

This is a limitation associated with using complete interferograms (up to 537,156 pixels). The RSS of two interferograms also cannot be compared, even for the same model geometry, for two reasons: The first is that each interferogram has a different number of coherent pixels, so that the number of data points differs between interferograms, and this will influence the RSS value. The second is that the RSS is also related to the magnitude of deformation that occurs in the interferogram but without a quantifiable relationship. Interferograms that involve little to no deformation may have very low RSS values while interferograms with significant deformation may have a higher RSS value, but actually provide a more realistic and better fit to the deformation source parameters. For these reasons statistical analysis of an overall best fit model to all of the data presented in this study cannot be performed, and we instead inspect the results from each model geometry for residual patterns (Figure 5), realistic source parameters, and consistently fit models throughout interferograms with significant deformation (Tables S6–S17).

As expected, the Mogi point source model does not converge consistently during the pre-2014 period (Table S6) due to time-varying atmospheric noise and a lack of observed volcanic deformation. The 2014 group of interferograms show more consistency, especially in the latitude and longitude (Figure 6), but the depth varies from ~3 to ~7 km bsl (Table S7). When interferograms are created using only images from 2014 with significant deformation, the depth and volume estimates begin to stabilize between 5 and 7 km bsl (Table S7). In 2015 the depths are generally estimated to be deeper for the interferograms with longer temporal baselines, which also have a worse fit than interferograms with shorter temporal baselines over the summer (Table S8). These summer interferograms have little deformation and are logically fit with very little volume change. The nonuniqueness of the depth and volume relationship is clear during these periods. Interferograms that span deformation that occurred in 2014 and 2015 show a range of point source depths from 6 to 10 km bsl, with a mean depth of ~8 km bsl (Figure 5, Tables 1 and S9). Generally, the parameters defined in the Mogi point source models are realistic and visual inspection of the model predictions and residuals show that a point source provides a good fit overall (Figure 5). The residual patterns exhibit small amounts of topographically correlated atmospheric effects that are most likely dominated by prevailing wind direction.

**Table 2**  
*Weighted Average Best Fit Okada Model Parameters for Each Group of Interferograms*

Group	Length (km)	Width (km)	Depth (km)	Dip (deg.)	Strike (deg.)	Longitude (dec. deg.)	Latitude (dec. deg.)	Opening (mm)	Volume (km <sup>3</sup> )
Pre-2014	1.38	9.05	6.3	58.9	256.8	179.591	51.953	6329	0.372
2014a	6.04	0.82	9.1	40.2	298.8	179.604	51.917	47,906	0.463
2014b	2.47	3.01	9.0	44.8	259.8	179.626	51.914	34,327	0.215
2015a	0.92	0.69	9.0	62.7	284.0	179.590	51.915	37,685	0.192
2015b	0.67	0.58	9.7	47.4	321.6	179.619	51.910	91,128	0.349
2014–2015	3.24	1.44	9.8	33.5	276.1	179.645	51.912	80,885	0.770

*Note.* Length is defined as the length of the dislocation plane in the strike direction, width is the distance down dip from the top of the plane to the bottom of the plane. Depth is defined as the location bsl of the center point on the bottom edge of the plane. Strike and dip motion on the plane is fixed to 0, so displacement can only be a result of opening (diking) motion.

**Table 3**  
Weighted Average Best Fit Yang Model Parameters for Each Group of Interferograms

Group	Longitude (dec. deg.)	Latitude (dec. deg.)	Depth (km)	Pressure Change (MPa)	Length of a (km)	Length of b (km)	Strike (deg.)	Plunge (deg.)	Volume (km <sup>3</sup> )
Pre-2014	179.602	51.981	2.6	0.599	2.95	0.55	132.9	14.2	0.001
2014a	179.618	51.934	8.6	15.064	4.12	0.97	138.8	46.2	0.043
2014b	179.622	51.918	6.7	2.242	5.65	0.81	72.0	37.1	0.010
2015a	179.656	51.932	7.9	28.431	1.19	0.62	206.0	5.7	0.029
2015b	179.602	51.938	5.8	1.815	4.61	1.57	95.8	61.2	0.005
2014–2015	179.641	51.936	8.1	42.731	1.43	0.85	157.2	42.3	0.056

Note. The a axis is the major axes, and the axis that the plunge is applied to. Because this is a spheroid, the b and c axes are the same length.

The Okada models produce much lower RSS values than the Mogi models, as expected, because there are nine parameters with which to fit the data rather than four (Table 2). Due to the time-varying atmospheric noise and lack of deformation, the pre-2014 interferograms are inconsistently fit by both large and small planes (lengths between 0.79 and 8 km and widths between 0.5 and 15 km) with depths that range from 3 to 10 km bsl (Table S10). This instability in parameter estimation for Okada solutions continues in the 2014 interferograms, with the exception of the depth parameter estimates that remain deep and often reach the upper boundary limit of 10 km bsl (Table S11). This depth limit is not adjusted further as the model depth

resolution is related to the surface deformation data coverage, in this case restricted by the size of the island (~20 km in diameter). The opening estimates are also extreme and unrealistic, with some reaching hundreds of meters, leading to similarly large volume changes. For 2015 and 2014–2015 data the Okada model fits the interferograms with a small plane at the boundary depth of 10 km but again with extreme and unrealistic opening values in the hundreds of meters (Tables S12 and S13). The weighted average parameter estimates for each group are not similar or indicative of any sort of trend except for a generally deeper source being fit with a large amount of volume change, signifying a poor overall fit of this model to the data (Table 2). The residual images for all interferograms have a radial pattern that the Okada model cannot resolve (Figure 5). Because the data are measured from a single viewing geometry, we cannot separate the horizontal and vertical components, and therefore discriminate between different source geometries. However, the large magnitude and spatial patterns of the Okada model residuals could not result simply from sensitivities to the horizontal and vertical deformation ratios, and we conclude that this geometry can be eliminated as a possible deformation model.

The Yang spheroid model results are very similar to the Mogi model results in best-fit spatial parameters but differ in RSS values and volume estimates. The majority of the models have major (a) and minor (b and c) axis lengths of 0.5–4.0 km. The pre-2014 interferograms are again inconsistently fit by either shallow depths with little volume change or a deeper source at the depth boundary limit of 10 km bsl with larger volume changes (Table S14). The 2014 interferograms consistently define a modeled source at 6–9 km bsl, with a weighted average volume influx of 0.043 km<sup>3</sup> (Tables 3 and S15). The source location shifts in the 2015 interferograms (Table S16) by a few kilometers to the northeast, and the depth and volume estimations decrease (by insignificant amounts) by the end of the summer. The deformation source location for the interferograms that span both the 2014 and 2015 inflation periods is shifted directly to the west of the 2015 location by 1 km, while the weighted average depth (8.1 km

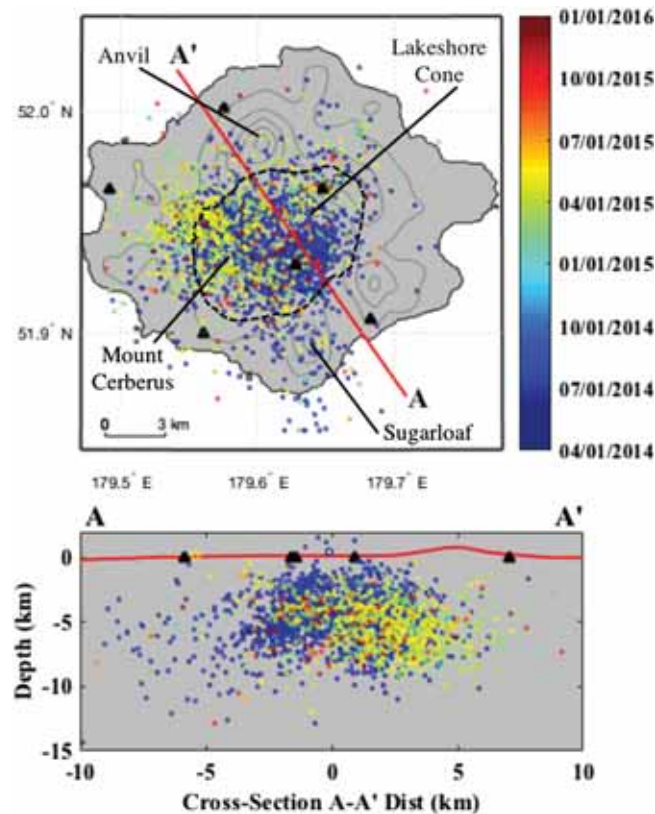


**Figure 6.** Map and depth locations of original AVO catalog hypocenters at Semisopochnoi from 2014 to 2015 (the temporal range of available interferograms). Locations of seismic stations are indicated with black triangles, main cones are labeled, and the dashed black line corresponds to the caldera as outlined in Figure 1.

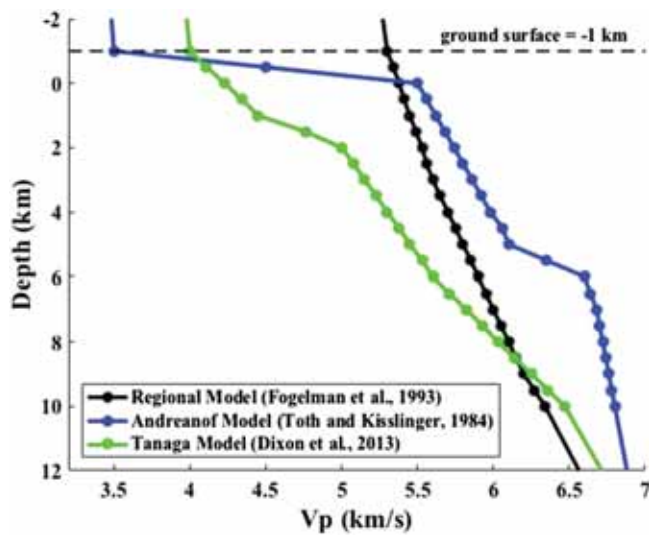


**Figure 7.** 1D velocity models appropriate for Semisopchnoi (Dixon et al., 2013; Fogleman et al., 1993; Toth & Kisslinger, 1984). Points indicate an inversion grid node within *tomoDD*. Note the wide range of  $V_p$ .  $V_s$  conversions use a  $V_p/V_s$  ratio of 1.78 in the Regional and Tanaga models and for the Andranof model 1.73 is used.

bsl) is closer to the 2014 deformation estimates. The volume calculated for this time period is larger while axes lengths are smaller (Tables S17), likely due to the large magnitude of deformation over these 2 years with no constraint on the spatial extent because Semisopchnoi is a small island. The interferogram group weighted averages show similar values for the spheroid latitude, longitude, depth, axes lengths, and plunge parameters, indicating some temporal stability (Table 3). The spheroid residuals are extremely low and indicate no systematic spatial patterns other than occasional atmospheric/topographic effects on the peaks of Anvil, Mount Cerberus, and Sugarloaf summits. The modeled and residual interferograms again indicate that the Yang source model is characterizing deformation adequately and that the SNR is not affected by atmospheric noise of a similar magnitude (Figure 6). The fringes that are modeled almost exactly match the number and pattern of the observed fringes in the interferograms, much like the Mogi model results.

#### 4. Seismic Analysis

Between 2012 and 2016, AVO located 2,636 earthquakes at Semisopchnoi (Cameron et al., 2017; Dixon et al., 2017) using the six local seismic stations (five short period, single component, and one broadband [CERB] three-component) and several other stations located on sur-

rounding islands (Figures 1, 2, and 6). The majority of events comprise the 2014 and 2015 swarms and are concentrated at mid- to shallow-crustal depths (0–9 km bsl) beneath the south-center of the island and the most recently active cones in the large caldera (Figure 6). Routine locations at Semisopchnoi are computed using AVO analyst verified and weighted  $P$  and  $S$  wave arrival times, static station corrections, and a one-dimensional regional velocity model (Fogleman et al., 1993; Figure 7).

Due to the difficulties of locating earthquakes along volcanic island arcs using small seismic networks, relative relocation methods have been applied at many Alaskan volcanoes to improve hypocenter precision (Buurman et al., 2013; DeShon et al., 2007; Johnson et al., 2010; Murphy et al., 2014; Ohlendorf et al., 2014; Pesicek et al., 2008; Ruppert et al., 2011; Statz-Boyer et al., 2009; Syracuse et al., 2011, 2015). Following on the success of many of these studies, we use the double-difference tomography algorithm *tomoDD* (Zhang & Thurber, 2003) combined with waveform cross-correlation (WCC) to minimize the difference between the observed and predicted travel times for pairs of events at common stations (i.e., differential times [DTs]), without the need for station corrections (Waldhauser, 2001). A hierarchical dynamic weighting scheme is applied that properly accounts for the varying data quality of the absolute travel time data derived from the AVO picks, and the catalog and WCC based DTs (Table S18). Following Pesicek et al. (2014), we use the program GISMO (Reyes & West, 2011) to compute the WCCs with 0.3 and 0.5 s windows around the  $P$  and  $S$  picks, respectively. Event pairs with WCC coefficients below 0.7 are excluded from the DT dataset. To increase the number of WCC derived  $S$  wave DTs, we use the 1D model (Figure 7) to predict  $S$  arrivals for stations lacking  $S$  picks and use the resulting arrival times to form windows for further WCC (Du et al., 2004; Pesicek et al., 2008). This allows us to increase the number of  $S$  wave DTs by a factor of 5. However,  $S$  wave DTs remain a minor percentage of the overall DTs used (~1%). In total, we use 14,095 direct  $P$  and  $S$  travel times, 207,598 catalog based differential times, and 382,163 WCC differential times to relocate the events at Semisopchnoi.

Location uncertainty is assessed by varying the 1D velocity model and perturbing initial hypocenter information (i.e., assuming pick times are 100% accurate). In addition to the Fogleman et al. (1993) velocity model that is routinely used, AVO has also published two, more regionally specific, one-dimensional velocity models that could be considered appropriate for Semisopchnoi (Toth & Kisslinger, 1984; Dixon et al., 2013; Figure 7). All three models are converted into gradients, the velocity model format used in *tomoDD*, and expanded into 3D velocity models using a coarse node spacing on the order of 100 s of kms and a fine node irregular spacing varying from 0.5 km under the summit to 5 km at the edges of the model (Text S3). In depth, nodes were placed every 0.5 km from the surface down to 10 km bsl with six additional deeper nodes at 15, 20,

**Table 4**

Mean Change and Standard Deviations (Std Dev) Between the Relocations and Initial AVO Data Using the AVO Regional Model (Fogleman et al., 1993), Andreatof and Tanaga Velocity Models

Data differenced	$\Delta$ Latitude (km)		$\Delta$ Longitude (km)		$\Delta$ Depth (km)		$\Delta$ Origin Time (sec)	
	Mean	Std Dev	Mean	Std Dev	Mean	Std Dev	Mean	Std Dev
AVO Initial Data <sup>a</sup>	0.01	1.23	-0.49	1.49	-0.18	1.56	-0.48	0.34
Andreatof Relocations <sup>b</sup>	0.06	0.43	0.03	0.55	0.00	0.85	-0.04	0.05
Tanaga Relocations <sup>c</sup>	-0.12	0.53	-0.18	0.70	0.43	0.95	0.13	0.08

<sup>a</sup>AVO regional model output—initial AVO data input. <sup>b</sup>AVO regional model output—Andreatof model output. <sup>c</sup>AVO regional model output—Tanaga model output.

25, 33, 47, and 65 km bsl (Figure 7). To account for topography the ground surface is defined to be 1 km above sea level. Changes in initial velocity model and node spacing yield epicentral locations, depths, and origin times with mean changes and standard deviations that exhibit little change between alternative velocity models, but measurable deviations from the original catalog times and locations of events (Table 4, Figure S19, and Text S3 for further details). Mapped locations using other models are provided in Figure S20. Placing all earthquakes at the cluster centroid within the Fogleman model rather than the AVO hypocenter yield a final earthquake dataset that varies from the final preferred earthquake catalog by a mean (standard deviation) of  $-0.06$  km ( $\pm 0.33$ ) latitude,  $-0.07$  km ( $\pm 0.34$ ) longitude,  $0.16$  km bsl ( $\pm 0.36$ ) depth, and  $0.05$  s ( $\pm 0.02$ ) origin time. Combined, these tests suggest absolute location uncertainties on the order of  $\sim 0.50$  km for epicenters,  $\sim 1.00$  km for depths, and  $0.07$  s for origin times.

An initial goal of the study was to resolve velocity perturbations below Semisopochnoi for comparison to deformation modeling results. Due to the small aperture of the local seismic network, the local earthquake tomography could be heavily biased by upgoing raypaths, so we conduct synthetic testing to explore sensitivity to subsurface velocity structure. We design a synthetic velocity model constructed by embedding a slow velocity region defined by best fit spheroid model parameters of the deformation source (Figure S21). This slow velocity region is embedded into the Fogleman et al. (1993) velocity model using a finer node spacing at depths of 6–10 km bsl with widths of 4 km in the east and north directions. Note that the finer node spacing expands the 1D velocity model into 3D by placing nodes in an irregular spacing varying from 0.5 km under the summit to 5 km at the edges of the model. *P* wave velocities for this region were fixed to be 20% slower than the original model. Synthetic travel times with up to 10% random noise and station noise are calculated to create a synthetic absolute travel time and differential time catalog that mimics the AVO catalog. Note that synthetic WCC data are not created. The synthetic time dataset is paired with the 1D Fogleman et al. (1993) model and inverted to jointly solve for earthquake location and velocity structure within *tomoDD*. However, the resultant model is little different from the starting 1D model, which indicates that few raypaths actually sample the depth range of interest (Figure S21), as expected given the depths of most hypocenters are above the depth of the modeled deformation source. The synthetic modeling also confirmed that tomographic inversion would be limited by the data geometry of the current dataset. Hence, we use *tomoDD* only as a DD location algorithm and fix the velocity model to the 1D Fogleman et al. (1993) solution for all relocation work such that only changes in hypocenter parameters ( $\Delta x$ ,  $\Delta y$ ,  $\Delta z$ ,  $\Delta t$ ) remain in the inverse problem.

Results of the relocation work reveal interesting subsurface features. Earthquakes occur under the central caldera and along the western section of the island. We find a linear aseismic zone within the distribution of earthquakes that trends southwest to northeast between Mount Cerberus and Sugarloaf regardless of which starting velocity models or grid configuration were used (Figures 7–9). Earthquakes recorded during the 2014 seismic swarm define the two boundaries of this dipping lineation (dark blue circles, Figure 8). The longer axis of this aseismic section is  $\sim 6$  km in the northeast-southwest direction, and the shorter axis is  $\sim 2$  km wide to the northwest-southeast (Figure 8). The aseismic feature extends from the surface to depths of 9–10 km bsl, which is also the lower boundary of the seismic cluster. Events in early to mid-2015

locate primarily on the west side of the aseismic zone but occur over the full depth range (green, yellow, and orange circles, Figure 8). Earthquakes in late 2015 and early 2016, however, occur near the deepest part of the seismogenic system (red circles, Figure 8).

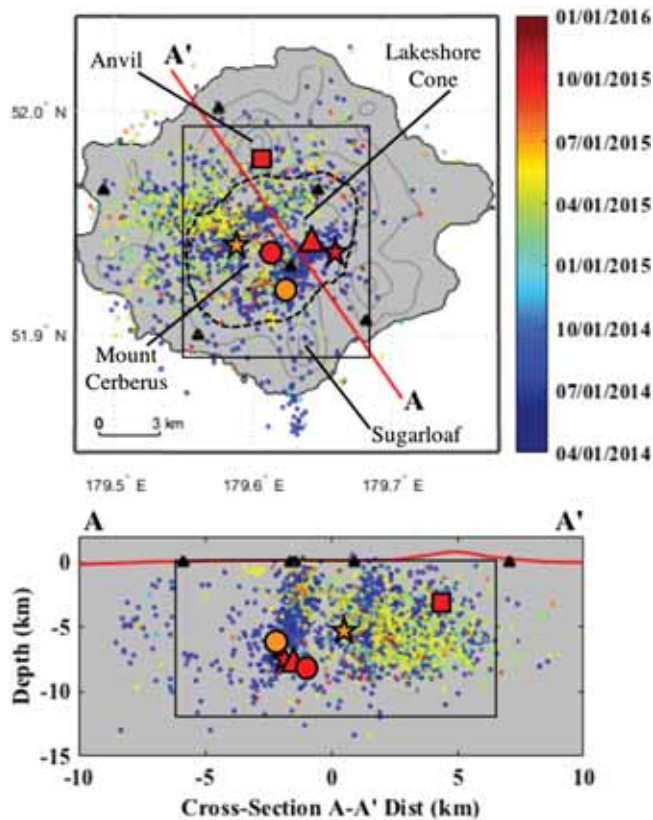


**Figure 8.** Map and depth relocations of seismic events from 2014 to 2015. The averaged best fit spheroid centroid locations for the pre-2014 (red square), 2014a, and 2014b (red and orange circles, respectively), 2015a and 2015b (red and orange stars, respectively), and 2014–2015 (red triangle) deformation source models are indicated. Black triangles are the locations of seismic stations, main eruptive cones are labeled, the dashed black circle corresponds to the caldera rim. Solid black boxes outline the area plotted in Figure 9.

## 5. Discussion

The aims of this paper are to investigate the magnitude and displacement rate at Semisopochnoi in 2014–2015 and to develop an interdisciplinary interpretation of magma storage dynamics for Semisopochnoi Volcano. We have presented seismic and geodetic data and analysis, but a recent geochemical publication (Coombs et al., 2018) provides additional constraints related to the storage and eruptive history at Semisopochnoi. We will first summarize these geochemical findings and then incorporate the interpretation published by Coombs et al. (2018) with the seismic and geodetic models resulting from this study. We then further assess the volume flux and displacement rate in comparison to other well-studied episodes of crustal magma intrusion. Finally, we discuss the value in measuring noneruptive deformation events as they relate to multiphysics numerical modeling of magma chambers and demonstrate the need for displacement measurements with high-temporal resolution to accurately constrain rheologic parameters of the surrounding crust.

### 5.1. Geochemical Data

Geochemical analysis of ignimbrite samples from Semisopochnoi's caldera-forming eruption describes compositions that were under ~2 kbar of pressure or at a depth of about 7 km bsl (Coombs et al., 2018). The source magmas for this eruption are described as having formed in the upper crust (<10 km bsl) at temperatures less than 900 °C and derived from a plagioclase-, amphibole-, and clinopyroxene-dominated crystal residue. Similar crystal-poor lavas with intermediate-composition were noted at Veniaminof Volcano in the eastern Aleutian arc and are interpreted to have segregated from the shallow region of a partial mush column (Bacon et al., 2007). Small cones, like Lakeshore Cone, dot the island and compositions of these low volume eruptions are interpreted to have tapped peripheral locations of this partial mush column. In the case of the monogenetic cones, crystal-rich basaltic andesites are suggested to have fractionated in the lower crust and the abundant phenocrysts grew during the ascent from these depths to the surface (Coombs et al., 2018). The Mount Cerberus cone complex geochemistry reflects a

series of magmas that followed a similar differentiation path, primarily formed by the crystallization of clinopyroxene-plagioclase gabbroic assemblage fractionated in the middle crust (Coombs et al., 2018). The pressure estimates for these eruptions fall between 2 and 4 kbar (depths of 7–15 km bsl), and the subtle compositional differences are interpreted as being sourced from discrete packages of deeper magma sources. Simultaneously to the Mount Cerberus eruptions, and more recently, Sugarloaf Peak has erupted crystal-rich high-alumina basalts that appear to have ascended from the deeper crust, bypassing the magmatic storage system that underlies the central caldera region (Coombs et al., 2018). These recent independent geochemical findings support both the tectonic interpretation of an extensional, rotating block and our geodetic and seismic evidence of a mid-crustal, partially molten magma storage zone.

### 5.2. Deformation Source

On the basis of the consistent radial pattern of uplift observed in the series of interferograms (Figures 5 and S4–S7) it is of little surprise that the Mogi point source (Mogi, 1958) and Yang spheroid (Yang et al., 1988) produced the most visually accurate estimates of surface deformation for all 66 of the modeled interferograms. The fit of these two models can be observed in the images of model residuals (Figure 5) and through the similarity in model parameters, as the latitude, longitude, and depth values estimated using the point source and spheroid models are much more realistic than the parameters used to fit the dislocation plane. The Okada dislocation plane has comparable RSS values to the spheroid model, but the modeled parameters are unrealistic and require a very deep and very large plane opening by magnitudes that would likely result in surface rupture, none of which was observed during these time periods. The difference between the

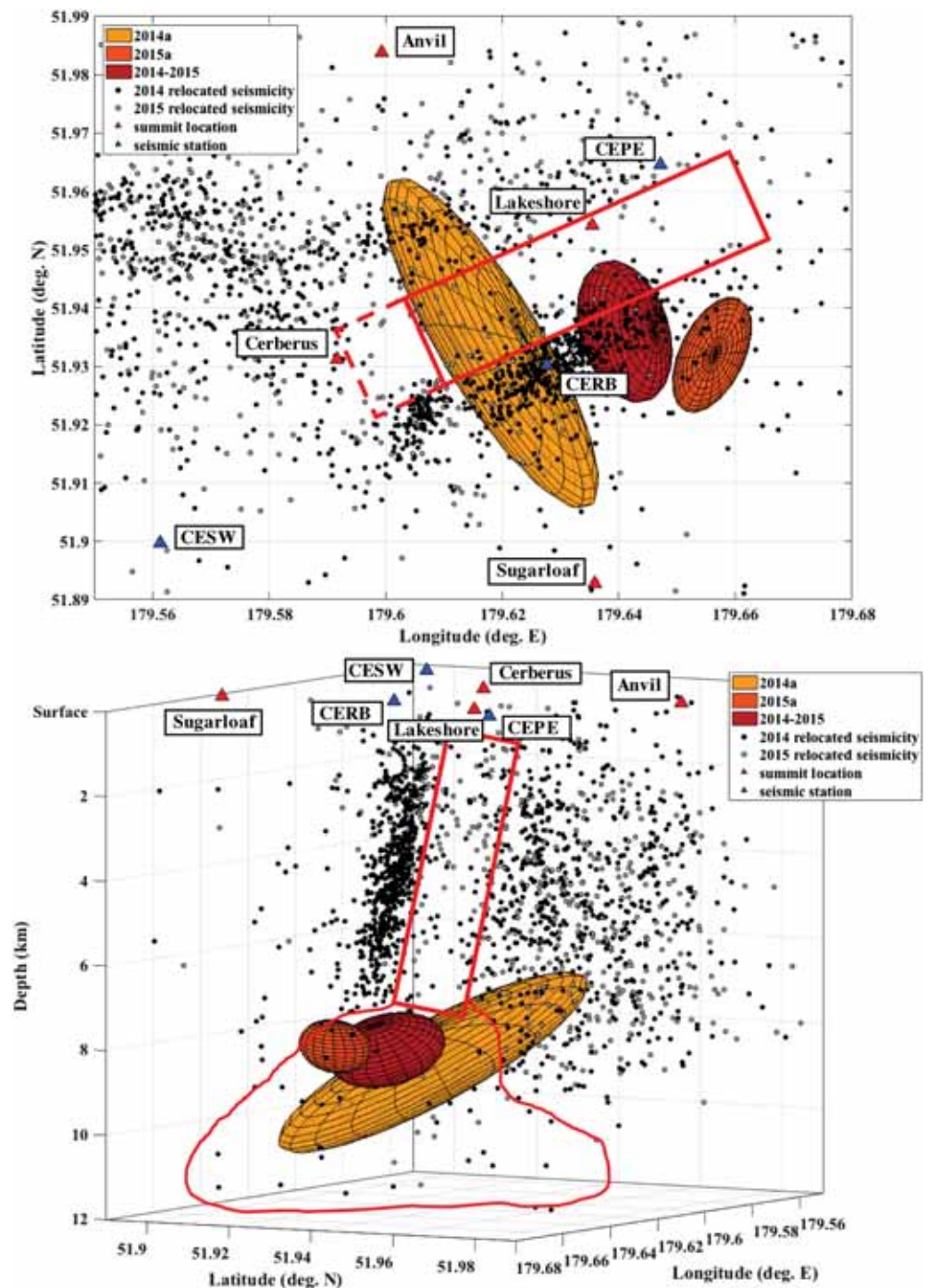


**Figure 9.** Best fit grouped weighted average spheroid source models are plotted with the relocated seismic events from 2014 and 2015. The pre-2014, 2014b, and 2015b inflation sources are not plotted because the lack of significant deformation resulted in inconsistent source parameters. The linear aseismic feature is well defined (red solid box) trending to the northeast in map view (top) and dipping to the southeast in the depth plot (bottom), with potential extensions farther to the southwest outlined with a dashed red box. An outline of the extension of this aseismic lineation to depth in relationship to the deformation models is also drawn as a red shape.

spheroid and point source model residuals appear to be negligible, and the spheroid is considered to be a more realistic representation of a magma storage geometry than a point source, so the best fit model preferred at Semisopchnoi is that of the averaged spheroid geometries with volume changes that are temporally dependent.

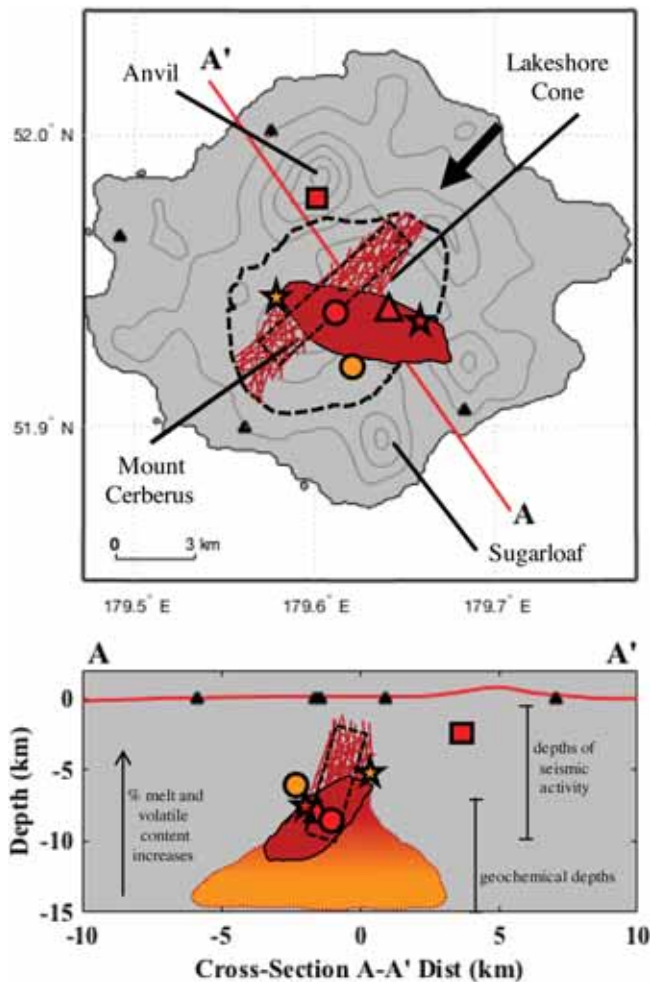


**Figure 10.** Conceptual model of the magma plumbing system at Semisopchnoi volcano as interpreted from seismic and surface deformation inversions for event locations, and source model parameters. Dark red shape is based on the averaged best fit spheroid models, with the red hash marks indicating the region of andesitic material with higher melt and volatile content coinciding with the aseismic region (outlined with a dashed black box). Depth profile is a complete view at depth from the northeast (black arrow, top panel). The orange to red gradation outlined with a red dashed line is our interpretation of deeper, lower melt content, basaltic crystal mush long term storage region (orange) interpreted from seismic locations and geochemical analysis. The caldera and main cones are outlined and labeled and the source centroid for the best fit spheroid models are plotted with the same conventions as Figure 8.

The best fit oblate spheroid with axes of approximately 4 and 1 km plunging at an angle of  $50^\circ$  is at a depth of  $\sim 8.6$  km bsl in 2014 and but relocates to a shallower depth of 7.9 km bsl in 2015 (Figures 8 and 9). This change in depth is assumed to be an artifact of model uncertainty, as the volume also decreases from 2014 to 2015. Regardless, the variability in volume and the similarity in location and geometry of this source through time indicates episodic inflation of an established storage region.

### 5.3. InSAR Data and Modelling Noise and Error Estimation

From the fundamental equation of SAR data (Lu & Dzurisin, 2014), it is clear that data uncertainty cannot be quantified from the measurements. This data uncertainty is compounded with differential SAR processing and deformation source model uncertainties, so that quantitative weights for each interferogram cannot be objectively established. Without a local GPS station, ascending data, weather measurements, or a nondeforming pixel, it is impossible to provide a meaningful estimate of data or processing error. There are a variety of methods used to estimate errors within interferograms (Bagnardi & Hooper, 2018; Biggs et al., 2010; Lohman & Simons, 2005), but these methods all require that a region of the interferogram exhibits no deformation. This requirement is not met in the interferograms presented here (Figures 3, 4, and S4–S7). Nevertheless, time series generation, interferogram stacking, weather models, semivariogram analysis, and quadtree subsampling techniques were all tested in an attempt to quantify noise, observe model parameter variance and covariance, and increase computational efficiency. Atmospheric noise is shown to be insignificant relative to the magnitude of deformation and use of time series, subsampling, stacking, or semivariogram models degraded the data or introduced additional errors and bias. None of these methods were applied, and all available data points from the original processed unwrapped interferograms were used for inversion modeling. Noise perturbations to the data were also used to test deformation source geometries, by adding in displacement measured from interferograms in 2011 and 2015 that showed no volcanic deformation. This method is based on the assumption that noise on Semisopchnoi Island is correlated in both space and time, but the modeling results showed that this is not the case, at Semisopchnoi during our study period. Further analysis and testing are beyond the scope of this study, but the InSAR data and supporting information form a basis for future work analyzing noise quantification, error estimation, and subsampling techniques applied to nonideal InSAR datasets.

### 5.4. Semisopchnoi Plumbing System

Using the deformation model and relocation results, paired with geochemical constraints from erupted products, we present a conceptual model for magma migration and storage at Semisopchnoi volcano during 2014 and 2015 (Figure 10). A large number of interferograms with little noise and high coherence allowed for the definition of a spheroid with a major axis of 4 km and minor axes averaging 1 km. This source of deformation is located under the center of the main caldera of Semisopchnoi at a depth of  $\sim 8.6$  km bsl, plunging  $\sim 50^\circ$  below the horizontal to the southeast.

Seismicity during the 2014 and 2015 seismic swarms falls into two linear patterns in the center of the caldera with radial, clustered activity in the western half of the island (Figures 8 and 9). The strong linear pattern of seismic events on the southeastern half of the caldera is steeply dipping to the southeast and a subtler delineation can be seen on the northwestern half of the caldera, with parallel strike and similar width and dip (Figures 7 and 8). These linear features are interpreted here to represent two fault zones that extend from the

deformation source to the ignimbrites of the caldera floor. The strike of both zones is perpendicular to the convergence direction and parallel to the NE-SW tectonic stresses associated with block rotation and extension along the oblique Aleutian subduction zone (Cross & Freymueller, 2008; Geist et al., 1988). The southeastern linear seismogenic feature is located directly above the spheroid that was found to best fit deformation observed from interferograms. The mid-2014 increase in seismic activity may represent fracturing along these fault zones due to stress increases resulting from a volume change of the spheroidal magma storage below (Figure 10) as other processes such as dike emplacement or fault slip would have altered the observed pattern of deformation. Additionally, separating these two linear features is a distinctly aseismic region (Figures 8 and 9).

We propose two interpretations of this linear aseismic zone beneath the center of the caldera. One interpretation is that the aseismic feature represents a region containing partial melt with a high concentration of volatiles that is unable to support brittle failure (Figure 10). This partial melt most likely increases in percent melt as depth decreases, due to the second boiling of the volatile saturated crystal mush that evolves from the stratification of the stored magma as crystallization differentiation of heavier mafic minerals at the bottom of the storage region leaves the lighter, more felsic, volatile rich material at shallower depths. This process can create a viscous and thermal environment that prohibits the accumulation of elastic stress required for seismic events to occur but may pressurize and transfer stress into the surrounding rock to produce high-frequency seismicity (e.g., Roman & Cashman, 2006). An alternative interpretation is that the aseismic feature represents fractured conduit fill from past eruptions that is still unable to support brittle failure. A fractured region located above the primary storage area that is bounded by two fault zones would provide a natural pathway for the upward migration of volatiles and ample pore pressure for groundwater storage. The presence of a fractured hydrothermal region such as this could also inhibit stress accumulation, regardless of the presence of partial melt. While this interpretation is possible, if the region was so heavily fractured that there was not enough brittle rock surface to allow for seismic activity, we would also expect it to respond to deformation very differently from the surrounding crust. This would be especially so with a highly fractured region that is as large as the aseismic zone mapped in this study (~6 by ~2 km). We see no evidence of this aseismic zone deforming at a different rate or pattern in the interferograms, and we believe the former interpretation to be more plausible than the later.

Fumarole activity at Semisopchnoi is nonexistent, but there is hot spring activity in Fenner Lake. The conduction of heat without any evidence of volatile exsolution supports the interpretation that an impermeable ignimbrite cap over the caldera floor could allow pressurization of the system by restricting the flow of volatiles, while still allowing for heat transfer to the surface. Geochemical evidence suggests that Semisopchnoi is underlain by a shallow magma reservoir with sufficiently long periods of quiescence so that crystallization differentiation occurs. The exsolution of volatiles associated with crystallization at the base of the storage region increases the volatile content at shallow depths, reducing the solidus so that the less dense felsic material exists as a partial melt (Bacon et al., 2007; Coombs et al., 2018). The aseismic zone defined in this study is large enough and located centrally in the caldera, so that it could be the direct representation of a shallow partial melt zone of a volatile saturated andesite resulting from crystallization differentiation at depth. A lack of seismicity continues to depths expected to coincide with the larger magma storage areas (~7–10 km bsl) (Figures 8–10), supporting the idea that a lack of seismicity at Semisopchnoi is an important signal for further constraining regions of magma storage.

The pattern of radially clustered seismic activity on the western half of the island may be a result of the stress regime associated with the linear fault zones in the caldera and regional tectonics. This older, weakened, cooler half of the island may be more likely to produce seismic events that lack a clear orientation or delineation. The apex of the plunging deformation source points directly at this cluster (Figure 9), which may indicate that the storage area is also focusing stress specifically in that direction.

The temporal resolution of the interferograms does not generally allow for direct comparison of deformation with seismic activity because of the limitation to summer acquisitions. There is, however, one interferogram with acquisition dates that span the decline in intensity of seismic activity from its maximum in 2014 (15 June 2014–26 June 2014). This interferogram exhibits the highest rate of deformation observed (~0.5 cm/day in the LOS, Figure 3) and occurs immediately after the peak in the number of daily seismic events (14 June 2014). Deformation that occurred before 15 June (~9 cm in the LOS, Figure 3) represents almost

a year of inflation, but since there was no seismic activity in 2013, the majority of this deformation may have occurred either immediately prior to the onset of seismicity or concurrently with the seismic swarm. The 2015 seismic activity occurred in the spring, when snow cover prevents the generation of interferograms from InSAR images, and hence these two interpretations cannot be resolved. All that can be stated with certainty regarding the relationship of seismic activity to deformation in 2015, is that by 25 June 2015 both seismic activity and deformation had ceased, with deformation having occurred at some point between 12 November 2014 and 25 June 2015 (Figures S6 and S7). The 2015 seismic activity, while of similar cumulative magnitude, had a greater spatial and temporal spread than the 2014 seismicity. The lower count of seismic events in 2015 also coincides with less observed surface deformation over the year, and therefore less volume change.

### 5.5. Volume Flux

To better investigate the episodic nature of intrusion at Semisopchnoi and volume flux into this magma storage region through time, an additional inversion using fixed parameters that reflect the averaged best-fit spheroid estimates of the 2014 and 2015 inversions is performed (centroid latitude and longitude location of 51.935°N and 179.630°E, major axis of 4 km, minor axes of 1 km, centroid depth of 8 km bsl, plunging at 50° below the horizontal to the southeast [N150°E]). The pressure (volume) parameter, however, was not fixed, so that this inversion estimated the change in volume through time of a fixed source. The large number of interferograms (and therefore models) evaluated for only 11 time steps means that commonly used linear least squares volume inversion methods (Biggs et al., 2010; Ji et al., 2018; Lu & Dzurisin, 2014; Lu, Masterlark, & Dzurisin, 2005) cannot be applied here, as the system is not linearly independent, rank deficient, and overdetermined.

Because of these limitations, in order to estimate an objective and complete volume change time series for Semisopchnoi Volcano from 2011 to 2015, cumulative volume change was calculated using all of the different combinations of interferograms that can be summed in series for each time step (SAR image acquisition date; Figure 11). The possible combinations of interferograms used to estimate cumulative volume increases in time, so to better understand the variability in these estimates the maximum and minimum cumulative volume of all of the possible interferogram combinations was also calculated at each time step. On the assumption that the most accurate estimate of volume change would come from the addition of volumes estimated from interferograms with the shortest temporal baseline (e.g., 20110805–20110816 + 20110816–20130811 + 20130811–20130822 ... etc.), a cumulative volume change time series from 2011 to 2015 is calculated (Figure 11 and Table 5). The cumulative volume flux estimated from fixed spheroid source parameters from 2011 to 2015 at Semisopchnoi is estimated to be about 0.074 km<sup>3</sup>, with a possible maximum of 0.089 km<sup>3</sup> and potentially as little as 0.037 km<sup>3</sup>. There are no time periods where subsidence was observed during this time, so it can be assumed that this volume was accumulated and is being stored at the depth and in the geometry defined in our source model.

When this volume analysis is compared to the grouped weighted average volume estimates for the best fit Yang spheroids (Table 3 and Figure 11), we see that the weighted averages for unrestricted model parameters fall between the shortest temporal baseline and maximum cumulative volume estimates when the input range is fixed. This indicates that the parameter values we use in the fixed model inversion are applicable to all of the time periods and provide a good source model approximation because the volume estimates are consistent between the fixed and freely fit models.

It is important to recall that because the LOS displacements in this study are relative to a moving point with unknown absolute displacement, the magnitudes of these measurements are underestimates of actual surface deformation and therefore the presented volume change time series is similarly underestimated. Similarly, model parameters (depth, pressure change, and axes lengths) could be affected by the lack of observable far-field deformation coupled with the lack of a stable reference point. Thus, future work to assess these effects using synthetic data sets is warranted.

### 5.6. Displacement Rate

Approximately half of all deformation events are intrusive (i.e., not immediately followed by an eruption (Biggs et al., 2014). Numerical models suggest that frequency of eruption is dependent on timescale of injection (Degruyter & Huber, 2014; Zhan & Gregg, 2019), particularly in smaller reservoirs (Gregg et al., 2013).

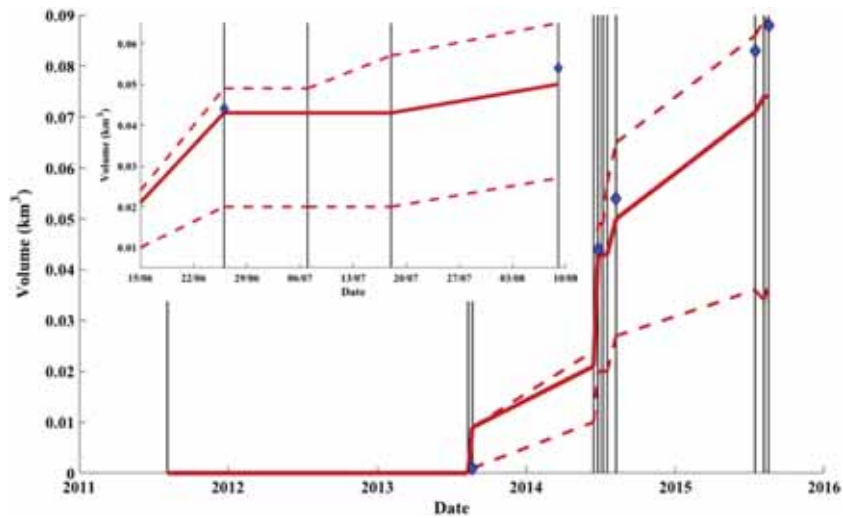


**Figure 11.** Cumulative volume using all the possible combinations of interferograms to construct a continuous time series. The solid black vertical lines are dates of SAR image acquisition, the thick red line is the cumulative volume using interferograms with the shortest temporal baselines (each primary image is used with the next acquisition as the secondary image). The dashed red lines are the maximum and minimum cumulative volume values from all of the potential interferogram combinations available at each image date (Table 5). Blue diamonds are the cumulative volume calculated from the grouped weighted averages from the best fit spheroid models (Table 3). Inset is a close up of the volume change in 2014 using the available images. Volume change in 2013 may be due to noise, but if it is due to actual deformation, uplift could have occurred between 2011 and 2013 and may be related to the 2012 seismic events.

However, it is unclear whether intrusive events are generally observed to have lower deformation rates than do episodes of intrusion that lead to eruption or if there is a threshold deformation rate for intrusion vs eruption. The temporal resolution of the TerraSAR-X data (11 days) for Semisopchnoi provides a unique opportunity to estimate more precise deformation rates than has previously been possible from InSAR analysis. At Semisopchnoi the deformation is large, but more notably, very rapid (max 0.5 cm/day in 2014). In this section we assess deformation rates at a range of representative volcanoes to determine whether the high deformation rate we observe at Semisopchnoi represents a maximum known value for an intrusive event.

We examine deformation rates at eight volcanoes listed in the Smithsonian Institution Global Volcanism Program Volcanoes of the World database (VOTW) as having an episode of deformation >10 cm

(Table 6). These volcanoes range from stratovolcanoes to shield volcanoes and result from hot spots, rifting, and subduction processes around the world (Bagnardi et al., 2013; Chadwick et al., 2006; Foumelis et al., 2013; González et al., 2013; Jay et al., 2014; Lu et al., 2005; Lu & Dzurisin, 2014; Pagli et al., 2012; Wicks et al., 2002). These measurements were made during preeruptive, posteruptive, and intereruptive deformation episodes. If given, we report the published value for the peak displacement rate of inflation events. If not reported, we calculate the deformation rate based on the image acquisition dates used to generate an interferogram and the total deformation. We note that many of these deformation episodes received considerable scientific and public attention, either due to the magnitude of deformation (e.g., Bagnardi et al., 2013; Lu, Wicks, et al., 2005) and/or the proximity of the volcano to a population center (e.g., Foumelis et al., 2013; Wicks et al., 2002).

From Table 6 it is clear that the inflation rate at Semisopchnoi is high, especially considering stratovolcanoes at subduction zones and the correlation with large inflation rates and eruption events (Foumelis et al., 2013; Jay et al., 2014; Lu, Wicks, et al., 2005; Wicks et al., 2002). This is a particularly rapid rate in the Aleutian arc (Lu, Wicks, et al., 2005), and

**Table 5**  
Table of Cumulative Volume Values (Figure 11)

Image date (yyyymmdd)	Cumulative volume (km <sup>3</sup> )		
	Maximum	Minimum	Shortest temporal baseline
20110805	0	0	----
20110816	0	0	0
20130811	0	0	0
20130822	0.009	0.001	0.009
20140615	0.024	0.010	0.021
20140626	0.049	0.020	0.043
20140707	0.049	0.020	0.043
20140718	0.057	0.020	0.043
20140809	0.065	0.027	0.050
20150716	0.086	0.036	0.071
20150807	0.089	0.034	0.074
20150818	0.089	0.037	0.074

*Note.* The maximum and minimum columns correspond to the dashed red lines, and the shortest temporal baseline value is the thick solid red line in Figure 11. The vertical black lines in Figure 11 represent the SAR image acquisition dates listed here.

**Table 6**  
Selected Volcanoes From a Query of the VOTW for Deformation of >10 cm

Volcano name	Inflation event (yyyy)	Satellite Revisit Period (days)	Duration (days)	Spatial extent (km)	Magnitude (cm)	Peak rate (mm/day)	Deformation type	Volcano type	Region	Region type
Sierra Negra <sup>a</sup>	2005	35	105	8	110	10	Preeruptive	Shield	Galapagos	Hot Spot
Fernandina <sup>b</sup>	2009	35	69	6	50	7	Preeruptive	Shield	Galapagos	Hot Spot
Puyehue-Cordon Caulle <sup>c</sup>	2013	1–48	312	20	38	4	Posteruptive	Stratovolcano	Southern Andes	Subduction
El Hierro <sup>d</sup>	2011	24 and 35	60	5	12	2	Preeruptive	Shield	Canary Islands	Hot Spot
Santorini <sup>e</sup>	2011–2012	24, 35, and 46	365	15	14	1	Intereruptive	Shield	Mediterranean	Subduction
Akutan <sup>f</sup>	1996–1996	35	623	10	51	1	Failed eruption	Stratovolcano	Aleutians	Subduction
Alu-Dalafilla <sup>g</sup>	2008–2010	35 and 46	651	10	90	1	Posteruptive	Stratovolcano	Erta Ale	Rifting
Three Sisters <sup>h</sup>	1996–2000	35	1505	20	10	0.08	Intereruptive	Stratovolcano	Cascadia	Subduction
Semisopochnoi <sup>i</sup>	2004–2010	35	2192	4	–6	–1	Intereruptive	Stratovolcano	Aleutians	Subduction
<b>Semisopochnoi</b>	<b>2014</b>	<b>11</b>	<b>363</b>	<b>&gt;20</b>	<b>17.1</b>	<b>6</b>	<b>Intereruptive</b>	<b>Stratovolcano</b>	<b>Aleutians</b>	<b>Subduction</b>
<b>Semisopochnoi</b>	<b>2015</b>	<b>11</b>	<b>341</b>	<b>&gt;20</b>	<b>7.8</b>	<b>0</b>	<b>Intereruptive</b>	<b>Stratovolcano</b>	<b>Aleutians</b>	<b>Subduction</b>

Note. Inflation event is the year(s) investigated in each reference and Satellite Revisit Period indicates the temporal resolution of the satellite data used for each study. Duration indicates the number of days of a measured episode of inflation. The Spatial Extent describes the longest axis of deformation, and Magnitude is the total uplift that occurred during the number of days indicated in Duration. Peak Rate is sometimes calculated directly using Duration and Magnitude, but when possible, the Peak Rate is taken from a published value, identified from an individual interferogram with a shorter time span than the Inflation Event, or analyzed in deformation time series plots and images. Deformation Type describes how the inflation is related to eruptions at each volcano and Volcano Type, Region, and Region Type are included to observe any correlation in deformation rate and location or volcanic formation.  
<sup>a</sup>Chadwick et al., 2006. <sup>b</sup>Bagnardi et al., 2013. <sup>c</sup>Jay et al., 2014. <sup>d</sup>González et al., 2013. <sup>e</sup>Foumelis et al., 2013. <sup>f</sup>Lu, Wicks, et al., 2005. <sup>g</sup>Pagli et al., 2012. <sup>h</sup>Wicks et al., 2002. <sup>i</sup>Lu & Dzurisin, 2014.

especially when considering the only other observation of deformation at this volcano (Lu & Dzurisin, 2014). The only volcanoes found to inflate more rapidly than Semisopochnoi are Sierra Negra (Chadwick et al., 2006) and Fernandina (Bagnardi et al., 2013) in the Galapagos. Both of these hot spot-generated shield volcanoes exhibited large scale deformation over a relatively small spatial area (mostly limited to their main calderas) in a short amount of time, immediately followed by a significant effusive eruption of basaltic lava (Bagnardi et al., 2013; Chadwick et al., 2006).

Many reported deformation rates may be limited (to minima) by the temporal limitations of InSAR data, as many studies are restricted to the interval of time defined by the satellite revisit period. Deformation may occur in 1–2 days, but because the temporal resolution is limited to 35 days at many of these volcanoes, this displacement rate will be calculated as an average over the entire 35-day period. This is the expected reason for the difference in peak rates between the 2014 and 2015 inflation episodes at Semisopochnoi, where 11-day resolution of deformation is observed from 15 June 2014 to 26 June 2014, but in 2015 the total deformation is averaged over the 10-month

interferogram from 09 August 2014 to 16 July 2015. Other geodetic data can provide the necessary temporal resolution to quantify maximum volcanic inflation rates globally, but these methods require ground-based efforts and are spatially limited, so that entire episodes or the maximum displacement is often not measured. InSAR methods provide a new basis to study this volcanic parameter that is valuable for defining volcanic processes and features such as the time to eruption onset, strength of the surrounding crust, viscosity and volatile content of magma, and evolution of a volcanic system. This study highlights the need for well-constrained global estimates of displacement rates during intrusive and pre-eruptive episodes and the benefit of satellites such as TerraSAR-X that have high temporal resolution.

## 6. Conclusions

Semisopochnoi volcano, though quite remote, can be observed and modeled using a combination of data transmitted from local and regional seismometers as well as data remotely sensed using SAR satellites. Data restrictions of one viewing geometry and a lack of GPS data prevented absolute measurements, but two episodes of inflation, in 2014 and 2015, are measured to have minimum cumulative uplift of ~25 cm with a peak rate of 6 mm/day during the end of a collocated seismic swarm in June 2014. Atmospheric errors range from 1 mm in the caldera floor where the maximum displacement occurred to 1 cm at relative high elevation locations. This topography- and turbulence-controlled noise was not characterized due to the nature of a temporally and spatially limited dataset. The island wide, LOS surface deformation at Semisopochnoi presents as a simple radial inflation pattern with a slight northeast-southwest oblique skew. Distinct periods of seismic swarm activity correlate in space with the surface deformation models inferred

from the inversion of surface displacement measurements created using differential SAR techniques. This inflation source is a reasonable approximation to the observed deformation, and modeled residuals show little to no additional systematic deformation beyond occasional low-magnitude atmospheric noise. The modeled interferograms are split into four different groups that allow for in depth analysis of the source parameters in the model based on temporal periods dictated by changes in seismic activity. The best fit model to characterize a deformation source at Semisopchnoi Volcano is described as an oblate spheroid. Relocation of the AVO catalog using waveform correlation and a relative relocation technique reveals a linear aseismic zone below the central caldera to depths of 10 km bsl. The feature is aligned with the expected tectonic regional stresses that are due to block expansion and rotation along the Aleutian trench. Tomographic inversions for velocity structure using current datasets cannot resolve velocity changes associated with modeled deformation sources.

While we cannot directly tie the seismic activity to the deformation temporally, the spatial patterns of both the deformation and the seismicity are individually similar in 2014 and 2015 (Figures 5 and 7) indicating that the seismogenic process and the mechanism responsible for surface deformation is the same for both years. We interpret these events to be linked through episodic influx of material from depth to a mid-crustal storage region (~8 km bsl). The largest flux of material (~0.043 km<sup>3</sup>) occurred in 2014, resulting in surface deformation of ~17 cm in the LOS direction, and a smaller pulse of material (~0.029 km<sup>3</sup>) occurred in 2015, producing ~8 cm of LOS deformation. The pressure associated with this flux of material is expected to have increased stresses above this area of magma storage so that the intracaldera faulting features, aligned with the NE-SW tectonic stress regime, producing the seismic pattern exhibited by our relocated hypocenters (Figures 7 and 10). Published geochemical data support both the tectonic interpretation of an extensional, rotating block and the geodetic and seismic evidence presented here for a midcrustal crystal-rich magma storage zone located centrally below the island with increasing percentages of melt and volatiles at the top of the storage system.

The magmatic system at Semisopchnoi is a geochemically complicated and active system that is controlled by a complex regional tectonic environment, not characteristic of the classic understanding of subduction processes. Geodetic models of surface deformation and seismic inversions for event locations often simplify or ignore the effect tectonic stress regimes produce within the model half-space. This study demonstrates that simple analytic models are not sufficient for characterizing volcanic dynamics, and there is a need to incorporate more realistic model environments. Better quantification of the location, geometry, pressure change, and stress distribution associated with magma storage in subduction related volcanic environments is required because controls such as tectonic stress, second boiling, and the potential for a viscoelastic cap can have a significant influence.

Semisopchnoi's dynamic magmatic system continues to produce swarms of microseismic events and exhibits large amounts of island wide inflation with no observed periods of deflation, subsidence, or eruptions. We know from its tectonic location on a segmentation boundary and the large volumes of past eruptions recorded in the geologic record that Semisopchnoi has infrequently produced large, explosive eruptions, and will likely do so again in the future if volatiles continue to exsolve at shallow depths but remain contained without any release of pressure. The system can be successfully monitored using methods that combine observations of surface deformation and seismicity in the future to further monitor these effects. These geophysical data and resulting models can be compared to storage depth estimates from geochemical analysis to create a comprehensive interdisciplinary interpretation of magma source dynamics. Future work combining earthquake and seismic ambient noise data could help better link changes in seismic velocity structure, earthquakes, and deformation data to further improve our understanding of the magmatic system and its relationship through time and space to the local tectonic stress distribution. For these reasons, the continued use of remote sensing tools and development of more realistic models at Semisopchnoi is essential.

## References

- Acocella, V., Di Lorenzo, R., Newhall, C., & Scandone, R. (2015). An overview of recent (1988 to 2014) caldera unrest: Knowledge and perspectives. *Reviews of Geophysics*, 53, 896–955. <https://doi.org/10.1002/2015RG000492>
- Bacon, C. R., Sisson, T. W., & Mazdab, F. K. (2007). Young cumulate complex beneath Veniaminof caldera, Aleutian arc, dated by zircon in erupted plutonic blocks. *Geology*, 35(6), 491–494.

## Acknowledgments

We thank Haijiang Zhang for providing access to *tomODD* version 10 as well as the associate editor, and two anonymous reviewers for their constructive comments regarding this work. We especially thank Michelle Coombs for her thorough comments and discussion relating the geochemical analysis to geodetic and seismic models that greatly improved this manuscript and solidified the interdisciplinary interpretation of magma storage. This research was financially supported by NASA Earth and Space Science Fellowship (NNX16AO26H), NASA Earth and Surface Interior Program (NNX14AQ95G) and the Shuler-Foscue Endowment at Southern Methodist University. Seismic data used in this study were collected by the AVO, a cooperation between the USGS, The University of Alaska, Fairbanks, and the Alaska Division of Geological and Geophysical Surveys. Any use of trade, firm, or product names is for descriptive purposes only and does not imply endorsement by the U.S. Government. Data for this study is publicly available online at <https://smu.box.com/s/rsqcm09ewnblhzvrmgf1jx6k3uu012l>.

- Bagnardi, M., Amelung, F., & Poland, M. P. (2013). A new model for the growth of basaltic shields based on deformation of Fernandina volcano, Galápagos Islands. *Earth and Planetary Science Letters*, 377, 358–366.
- Bagnardi, M., & Hooper, A. (2018). Inversion of surface deformation data for rapid estimates of source parameters and uncertainties: A Bayesian approach. *Geochemistry, Geophysics, Geosystems*, 19, 2194–2211. <https://doi.org/10.1029/2018GC007585>
- Berardino, P., Fornaro, G., Lanari, R., & Sansosti, E. (2002). A new algorithm for surface deformation monitoring based on small baseline differential SAR interferograms. *IEEE Transactions on Geoscience and Remote Sensing*, 40(11), 2375–2383.
- Biggs, J., Ebmeier, S. K., Aspinall, W. P., Lu, Z., Pritchard, M. E., Sparks, R. S. J., & Mather, T. A. (2014). Global link between deformation and volcanic eruption quantified by satellite imagery. *Nature communications*, 5, 3471.
- Biggs, J., Lu, Z., Fournier, T., & Freymueller, J. T. (2010). Magma flux at Okmok Volcano, Alaska, from a joint inversion of continuous GPS, campaign GPS, and interferometric synthetic aperture radar. *Journal of Geophysical Research*, 115, B12401. <https://doi.org/10.1029/2010JB007577>
- Biggs, J., & Pritchard, M. E. (2017). Global volcano monitoring: What does it mean when volcanoes deform? *Elements*, 13(1), 17–22.
- Buurman, H., West, M. E., & Roman, D. C. (2013). Using repeating volcano-tectonic earthquakes to track post-eruptive activity in the conduit system at Redoubt Volcano, Alaska. *Geology*, 41(4), 511–514.
- Cameron, C. E., Dixon, J. P., Neal, C. A., Waythomas, C.F., Schaefer, J. R., & McGimsey, R. G. (2017). 2014 Volcanic activity in Alaska—Summary of events and response of the Alaska Volcano Observatory: U.S. Geological Survey Scientific Investigations Report 2017-5077, 81 p., <https://doi.org/10.3133/sir20175077>.
- Chadwick, W. W. Jr., Geist, D. J., Jónsson, S., Poland, M., Johnson, D. J., & Meertens, C. M. (2006). A volcano bursting at the seams: Inflation, faulting, and eruption at Sierra Negra volcano, Galápagos. *Geology*, 34(12), 1025–1028.
- Coats, R. R. (1959). Geologic reconnaissance of Semisopochnoi Island, Western Aleutian Islands: U.S. Geologic Survey Bulletin 1028-O.
- Coombs, M. L., Larsen, J. F., & C. A. Neal (2018). Postglacial eruptive history and geochemistry of Semisopochnoi volcano, western Aleutian Islands, Alaska (Scientific Investigations Report No. 2017-5150). US Geological Survey. <https://doi.org/10.3133/sir20175150>
- Cooper, A. K., Marlow, M. S., & Ben-Avraham, Z. V. I. (1981). Multichannel seismic evidence bearing on the origin of Bowers Ridge, Bering Sea. *Geological Society of America Bulletin*, 92(7), 474–484.
- Cross, R. S., & Freymueller, J. T. (2008). Evidence for and implications of a Bering plate based on geodetic measurements from the Aleutians and western Alaska. *Journal of Geophysical Research*, 113, B07405. <https://doi.org/10.1029/2007JB005136>
- DeGrandpre, K., Wang, T., Lu, Z., & Freymueller, J. T. (2017). Episodic inflation and complex surface deformation of Akutan volcano, Alaska revealed from GPS time-series. *Journal of Volcanology and Geothermal Research*, 347, 337–359.
- Degruyter, W., & Huber, C. (2014). A model for eruption frequency of upper crustal silicic magma chambers. *Earth and Planetary Science Letters*, 403, 117–130.
- Delong, S. E., Perfit, M. R., McCulloch, M. T., & Ach, J. (1985). Magmatic evolution of Semisopochnoi Island, Alaska: Trace-element and isotopic constraints. *The Journal of Geology*, 93(5), 609–618.
- DeShon, H. R., Thurber, C. H., & Rowe, C. (2007). High-precision earthquake location and three-dimensional P wave velocity determination at Redoubt Volcano, Alaska. *Journal of Geophysical Research*, 112, B07312. <https://doi.org/10.1029/2006JB004751>
- Dixon, J. P., Cameron, C. E., Iezzi, A. M., & Wallace, K. (2017). 2015 Volcanic activity in Alaska—Summary of events and response of the Alaska Volcano Observatory: U.S. Geological Survey Scientific Investigations Report 2017-5104, 61 p., <https://doi.org/10.3133/sir20175104>.
- Dixon, J. P., Stihler, S. D., Power, J. A., Haney, M., Parker, T., Searcy, C. K., & Prejean, S. (2013). Catalog of earthquake hypocenters at Alaskan volcanoes: January 1 through December 31, 2012: U.S. Geological Survey Data Series 789, 84 p., <http://pubs.usgs.gov/ds/789/>
- Du, W., Thurber, C. H., Reyners, M., Eberhart-Phillips, D., & Zhang, H. (2004). New constraints on seismicity in the Wellington region of New Zealand from relocated earthquake hypocenters. *Geophysical Journal International*, 158(3), 1088–1102. <https://doi.org/10.1111/j.1365-246X.2004.02366.x>
- Ebmeier, S. K., Andrews, B. J., Araya, M. C., Arnold, D. W. D., Biggs, J., Cooper, C., et al. (2018). Synthesis of global satellite observations of magmatic and volcanic deformation: implications for volcano monitoring & the lateral extent of magmatic domains. *Journal of Applied Volcanology*, 7(1), 2.
- Fogleman, K. A., Lahr, J. C., Stephens, C. D., & Page, R.A. (1993). Earthquake locations determined by the southern Alaska seismograph network for October 1971 through May 1989.
- Foster, J., Kealy, J., Cherubini, T., Businger, S., Lu, Z., & Murphy, M. (2013). The utility of atmospheric analyses for the mitigation of artifacts in InSAR. *Journal of Geophysical Research: Solid Earth*, 118, 748–758. <https://doi.org/10.1002/jgrb.50093>
- Foumelis, M., Trasatti, E., Papageorgiou, E., Stramondo, S., & Parcharidis, I. (2013). Monitoring Santorini volcano (Greece) breathing from space. *Geophysical Journal International*, 193(1), 161–170.
- Fournier, T. J., Pritchard, M. E., & Riddick, S. N. (2010). Duration, magnitude, and frequency of subaerial volcano deformation events: New results from Latin America using InSAR and a global synthesis. *Geochemistry, Geophysics, Geosystems*, 11, Q01003. <https://doi.org/10.1029/2009GC002558>
- Geist, E. L., Childs, J. R., & Scholl, D. W. (1988). The origin of summit basins of the Aleutian Ridge: Implications for block rotation of an arc massif. *Tectonics*, 7(2), 327–341.
- González, P. J., Samsonov, S. V., Pepe, S., Tiampo, K. F., Tizzani, P., Casu, F., et al. (2013). Magma storage and migration associated with the 2011–2012 El Hierro eruption: Implications for crustal magmatic systems at oceanic island volcanoes. *Journal of Geophysical Research: Solid Earth*, 118, 4361–4377. <https://doi.org/10.1002/jgrb.50289>
- Gregg, P. M., De Silva, S. L., & Grosfils, E. B. (2013). Thermomechanics of shallow magma chamber pressurization: Implications for the assessment of ground deformation data at active volcanoes. *Earth and Planetary Science Letters*, 384, 100–108.
- Grosse, P., Euillades, P. A., Euillades, L. D., & de Vries, B. V. W. (2014). A global database of composite volcano morphometry. *Bulletin of Volcanology*, 76(1), 784.
- Jay, J., Costa, F., Pritchard, M., Lara, L., Singer, B., & Herrin, J. (2014). Locating magma reservoirs using InSAR and petrology before and during the 2011–2012 Cordón Caulle silicic eruption. *Earth and Planetary Science Letters*, 395, 254–266.
- Ji, L., Izbekov, P., Senyukov, S., & Lu, Z. (2018). Deformation patterns, magma supply, and magma storage at Karymsky Volcanic Center, Kamchatka, Russia, 2000–2010, revealed by InSAR. *Journal of Volcanology and Geothermal Research*, 352, 106–116.
- Johnson, J. H., Prejean, S., Savage, M. K., & J. Townend (2010). Anisotropy, repeating earthquakes, and seismicity associated with the 2008 eruption of Okmok volcano, Alaska. *Journal of Geophysical Research*, 115, B00B04. <https://doi.org/10.1029/2009JB006991>
- Kienle, J. (1971). Gravity and magnetic measurements over Bowers ridge and Shirshov ridge, Bering Sea. *Journal of Geophysical Research*, 76(29), 7138–7153.
- Kinoshita, Y., Furuya, M., Hobiger, T., & Ichikawa, R. (2013). Are numerical weather model outputs helpful to reduce tropospheric delay signals in InSAR data? *Journal of Geodesy*, 87(3), 267–277.

- Le Mével, H., Feigl, K. L., Córdova, L., DeMets, C., & Lundgren, P. (2015). Evolution of unrest at Laguna del Maule volcanic field (Chile) from InSAR and GPS measurements, 2003 to 2014. *Geophysical Research Letters*, *42*, 6590–6598. <https://doi.org/10.1002/2015GL064665>
- Lee, C. W., Lu, Z., Jung, H. S., Won, J. S., & Dzurisin, D. (2006). Surface deformation of Augustine Volcano, 1992–2005, from multiple-interferogram processing using a refined small baseline subset (SBAS) interferometric synthetic aperture radar (InSAR) approach. The 2006 eruption of Augustine Volcano, Alaska: U.S. Geological Survey Professional Paper 1769, 453–465.
- Lee, C. W., Lu, Z., Won, J. S., Jung, H. S., & Dzurisin, D. (2013). Dynamic deformation of Seguam Island, Alaska, 1992–2008, from multi-interferogram InSAR processing. *Journal of Volcanology and Geothermal Research*, *260*, 43–51.
- Lohman, R. B., & Simons, M. (2005). Some thoughts on the use of InSAR data to constrain models of surface deformation: Noise structure and data downsampling. *Geochemistry, Geophysics, Geosystems*, *6*, Q01007. <https://doi.org/10.1029/2004GC000841>
- Lu, Z., & Dzurisin, D. (2010). Ground surface deformation patterns, magma supply, and magma storage at Okmok volcano, Alaska, from InSAR analysis: 2. Coeruptive deflation, July–August 2008. *Journal of Geophysical Research*, *115*, B00B03. <https://doi.org/10.1029/2009JB006970>
- Lu, Z., & Dzurisin, D. (2014). *In SAR imaging of Aleutian volcanoes: Monitoring a volcanic arc from space*. Berlin, Heidelberg: Springer Science & Business Media.
- Lu, Z., Dzurisin, D., Wicks, C., Power, J., Kwoun, O., & Rykhus, R. (2007). Diverse deformation patterns of Aleutian volcanoes from satellite interferometric synthetic aperture radar (InSAR). *Volcanism and subduction: The Kamchatka region*, 249–261.
- Lu, Z., Masterlark, T., & Dzurisin, D. (2005). Interferometric synthetic aperture radar study of Okmok volcano, Alaska, 1992–2003: Magma supply dynamics and postemplacement lava flow deformation. *Journal of Geophysical Research*, *110*, B02403. <https://doi.org/10.1029/2004JB003148>
- Lu, Z., Masterlark, T., Dzurisin, D., Rykhus, R., & Wicks, C. (2003). Magma supply dynamics at Westdahl volcano, Alaska, modeled from satellite radar interferometry. *Journal of Geophysical Research*, *108*(B7), 2354. <https://doi.org/10.1029/2002JB002311>
- Lu, Z., Masterlark, T., Power, J., Dzurisin, D., & Wicks, C. (2002). Subsidence at Kiska volcano, western Aleutians, detected by satellite radar interferometry. *Geophysical Research Letters*, *29*(18), 1855. <https://doi.org/10.1029/2002GL014948>
- Lu, Z., Wicks, C. Jr., Kwoun, O., Power, J. A., & Dzurisin, D. (2005). Surface deformation associated with the March 1996 earthquake swarm at Akutan Island, Alaska, revealed by C-band ERS and L-band JERS radar interferometry. *Canadian Journal of Remote Sensing*, *31*(1), 7–20.
- Ludwig, W. J., Murauchi, S., Den, N., Ewing, M., Hotta, H., Houtz, R. E., et al. (1971). Structure of Bowers Ridge, Bering Sea. *Journal of Geophysical Research*, *76*(26), 6350–6366.
- Lundgren, P., Casu, F., Manzo, M., Pepe, A., Berardino, P., Sansosti, E., & Lanari, R. (2004). Gravity and magma induced spreading of Mount Etna volcano revealed by satellite radar interferometry. *Geophysical Research Letters*, *31*, L04602. <https://doi.org/10.1029/2003GL018736>
- Massonnet, D., & Feigl, K. L. (1998). Radar interferometry and its application to changes in the Earth's surface. *Reviews of geophysics*, *36*(4), 441–500.
- Masterlark, T., Feigl, K. L., Haney, M., Stone, J., Thurber, C., & Ronchin, E. (2012). Nonlinear estimation of geometric parameters in FEMs of volcano deformation: Integrating tomography models and geodetic data for Okmok Volcano, Alaska. *Journal of Geophysical Research*, *117*, B02407. <https://doi.org/10.1029/2011JB008811>
- Mogi, K. (1958). Relations between the eruptions of various volcanoes and the deformations of the ground surfaces around them.
- Moran, S. C., Kwoun, O., Masterlark, T., & Lu, Z. (2006). On the absence of InSAR-detected volcano deformation spanning the 1995–1996 and 1999 eruptions of Shishaldin Volcano, Alaska. *Journal of Volcanology and Geothermal Research*, *150*(1–3), 119–131.
- Moran, S. C., Newhall, C., & Roman, D. C. (2011). Failed magmatic eruptions: Late-stage cessation of magma ascent. *Bulletin of Volcanology*, *73*(2), 115–122.
- Murphy, R., Thurber, C., Prejean, S., & Bennington, N. (2014). Three-dimensional seismic velocity structure and earthquake relocations at Katmai, Alaska. *Journal of Volcanology and Geothermal Research*, *276*, 121–131.
- National Academies of Sciences, Engineering, and Medicine (2017). *Volcanic eruptions and their repose, unrest, precursors, and timing*. Washington, District of Columbia: National Academies Press.
- Ohlendorf, S. J., Thurber, C. H., Pesicek, J. D., & Prejean, S. G. (2014). Seismicity and seismic structure at Okmok Volcano, Alaska. *Journal of Volcanology and Geothermal Research*, *278*, 103–119.
- Okada, Y. (1985). Surface deformation due to shear and tensile faults in a half-space. *Bulletin of the seismological society of America*, *75*(4), 1135–1154.
- Pagli, C., Wright, T. J., Ebinger, C. J., Yun, S. H., Cann, J. R., Barnie, T., & Ayele, A. (2012). Shallow axial magma chamber at the slow-spreading Erta Ale Ridge. *Nature Geoscience*, *5*(4), 284.
- Parker, A. L., Biggs, J., Walters, R. J., Ebmeier, S. K., Wright, T. J., Teanby, N. A., & Lu, Z. (2015). Systematic assessment of atmospheric uncertainties for InSAR data at volcanic arcs using large-scale atmospheric models: Application to the Cascade volcanoes, United States. *Remote Sensing of Environment*, *170*, 102–114.
- Pesicek, J., Child, D., Artman, B., & Cieřlik, K. (2014). Picking versus stacking in a modern microearthquake location: Comparison of results from a surface passive seismic monitoring array in Oklahoma. *Geophysics*, *79*(6), KS61–KS68. <https://doi.org/10.1190/geo2013-0404.1>
- Pesicek, J. D., Thurber, C. H., DeShon, H. R., Prejean, S. G., & Zhang, H. (2008). Three-dimensional P-wave velocity structure and precise earthquake relocation at Great Sitkin Volcano, Alaska. *Bulletin of the Seismological Society of America*, *98*(5), 2428–2448.
- Pritchard, M. E., Biggs, J., Wauthier, C., Sansosti, E., Arnold, D. W., Delgado, F., et al. (2018). Towards coordinated regional multi-satellite InSAR volcano observations: Results from the Latin America pilot project. *Journal of Applied Volcanology*, *7*(1), 5.
- Rabinowitz, P. D. (1974). Seismic profiling between Bowers ridge and Shirshov ridge in the Bering Sea. *Journal of Geophysical Research*, *79*(32), 4977–4979.
- Reath, K., Pritchard, M., Poland, M., Delgado, F., Carn, S., Coppola, D., et al. (2019). Thermal, deformation, and degassing remote sensing time series (CE 2000–2017) at the 47 most active volcanoes in Latin America: implications for volcanic systems. *Journal of Geophysical Research: Solid Earth*, *124*, 195–218. <https://doi.org/10.1029/2018JB016199>
- Reyes, C. G., & West, M. E. (2011). The waveform suite: A robust platform for manipulating waveforms in MATLAB. *SRL*, *82*(1), 104–110.
- Roman, D. C., & Cashman, K. V. (2006). The origin of volcano-tectonic earthquake swarms. *Geology*, *34*(6), 457–460.
- Ruppert, N. A., Prejean, S., & Hansen, R. A. (2011). Seismic swarm associated with the 2008 eruption of Kasatochi Volcano, Alaska: Earthquake locations and source parameters. *Journal of Geophysical Research*, *116*, B00B07. <https://doi.org/10.1029/2010JB007435>
- Scholl, D. W., Vallier, T. L., & Stevenson, A. J. (1986). Terrane accretion, production, and continental growth: A perspective based on the origin and tectonic fate of the Aleutian–Bering Sea region. *Geology*, *14*(1), 43–47.

- Statz-Boyer, P., Thurber, C., Pesicek, J., & Prejean, S. (2009). High precision relocation of earthquakes at Iliamna Volcano, Alaska. *Journal of Volcanology and Geothermal Research*, 184(3), 323–332.
- Stix, J., & de Moor, J. M. (2018). Understanding and forecasting phreatic eruptions driven by magmatic degassing. *Earth, Planets and Space*, 70(1), 83.
- Syracuse, E. M., Maceira, M., Zhang, H., & Thurber, C. H. (2015). Seismicity and structure of Akutan and Makushin Volcanoes, Alaska, using joint body and surface wave tomography. *Journal of Geophysical Research: Solid Earth*, 120, 1036–1052. <https://doi.org/10.1002/2014JB011616>
- Syracuse, E. M., Thurber, C. H., & Power, J. A. (2011). The Augustine magmatic system as revealed by seismic tomography and relocated earthquake hypocenters from 1994 through 2009. *Journal of Geophysical Research*, 116, B09306. <https://doi.org/10.1029/2010JB008129>
- Toth, T., & Kisslinger, C. (1984). Revised focal depths and velocity model for local earthquakes in the Adak seismic zone. *Bulletin of the Seismological Society of America*, 74(4), 1349–1360.
- Waldhauser, F. (2001). HypoDD-A program to compute double-difference hypocenter locations (No. 2001-113).
- Waldhauser, F., & Ellsworth, W. L. (2000). A double-difference earthquake location algorithm: Method and application to the northern Hayward fault, California. *Bulletin of the Seismological Society of America*, 90(6), 1353–1368.
- Wang, T., DeGrandpre, K., Lu, Z., & Freymueller, J. T. (2018). Complex surface deformation of Akutan volcano, Alaska revealed from InSAR time series. *International Journal of Applied Earth Observation and Geoinformation*, 64, 171–180.
- Wanke, M., Portnyagin, M., Hoernle, K., Werner, R., Hauff, F., van den Bogaard, P., & Garbe-Schönberg, D. (2012). Bowers Ridge (Bering Sea): An Oligocene–Early Miocene island arc. *Geology*, 40(8), 687–690.
- Webster, R., & Oliver, M. A. (2007). *Geostatistics for environmental scientists*. West Sussex, England: John Wiley & Sons.
- Wegmuller, U. (1997). Gamma SAR processor and interferometry software. In Proc. the 3rd ERS Symposium, ESA, 1997 (pp. 1686–1692).
- Wegmuller, U., Werner, C., & Strozzi, T. (1998). SAR interferometric and differential interferometric processing chain. In Geoscience and Remote Sensing Symposium Proceedings, 1998. IGARSS'98. 1998 IEEE International (Vol. 2, pp. 1106–1108). IEEE.
- Wicks, C. W. Jr., Dzurisin, D., Ingebritsen, S., Thatcher, W., Lu, Z., & Iverson, J. (2002). Magmatic activity beneath the quiescent Three Sisters volcanic center, central Oregon Cascade Range, USA. *Geophysical Research Letters*, 29(7), 1122. <https://doi.org/10.1029/2001GL014205>
- Williams, C. A., & Wadge, G. (1998). The effects of topography on magma chamber deformation models: Application to Mt. Etna and radar interferometry. *Geophysical Research Letters*, 25(10), 1549–1552.
- Yang, X. M., Davis, P. M., & Dieterich, J. H. (1988). Deformation from inflation of a dipping finite prolate spheroid in an elastic half-space as a model for volcanic stressing. *Journal of Geophysical Research*, 93(B5), 4249–4257.
- Yu, C., Li, Z., & Penna, N. T. (2018). Interferometric synthetic aperture radar atmospheric correction using a GPS-based iterative tropospheric decomposition model. *Remote Sensing of Environment*, 204. <https://doi.org/10.1016/j.rse.2017.10.038>
- Yu, C., Li, Z., Penna, N. T., & Crippa, P. (2018). Generic atmospheric correction model for Interferometric Synthetic Aperture Radar observations. *Journal of Geophysical Research: Solid Earth*, 123, 9202–9222. <https://doi.org/10.1029/2017JB015305>
- Yu, C., Penna, N. T., & Li, Z. (2017). Generation of real-time mode high-resolution water vapor fields from GPS observations. *Journal of Geophysical Research: Atmospheres*, 122, 2008–2025. <https://doi.org/10.1002/2016JD025753>
- Zhan, Y., & Gregg, P. M. (2019). How accurately can we model magma reservoir failure with uncertainties in host-rock rheology? *Journal of Geophysical Research: Solid Earth*. <https://doi.org/10.1029/2019JB018178>
- Zhang, H., & Thurber, C. (2003). Double-difference tomography: the method and its application to the Hayward fault, California. *Bulletin of the Seismological Society of America*, 93, 1875–1889.
- Zhang, H., & Thurber, C. (2006). Development and applications of double-difference seismic tomography. *Pure and Applied Geophysics*, 163(2-3), 373–340.